Università di Napoli Federico II – Scuola Superiore Meridionale

PhD Program in Genomic and Experimental Medicine (GEM)

Host Cell Remodelling during SARS-CoV-2 Infection: Mechanistic Insights into Autophagy and ER-Driven Membrane Rearrangements.

Dissecting the Role of Autophagy-Related Factors and Atlastin-Mediated ER Dynamics in Double-Membrane Vesicle Biogenesis

A dissertation presented by

Mgr. Štěpánka Vlachová

Matriculation number: DR995934

in partial fulfilment of the requirements for the degree of

Doctor of Philosophy

in

Genomic and Experimental Medicine (GEM)- 37º Cycle

Dissertation Advisor: Professor Mirko Cortese, PhD

Dissertation Advisor: Professor Lina Herhaus, PhD

October 2025

GEM program coordinator:

Prof. Brunella Franco, MD.,

Professor of Medical Genetics

Department of Translational Medicine

Università di Napoli Federico II

Principal Investigator- Telethon Institute of Genetics and Medicine (TIGEM)

Abstract

Positive-sense single-stranded RNA (+ssRNA) viruses, including SARS-CoV-2, are known to extensively remodel host cell membranes to establish viral replication organelles, which have the form of double-membrane vesicles (DMVs) in case of Coronaviruses. While viral non-structural proteins are known to drive DMV biogenesis, the contribution of host factors remains mostly elusive. Here, we identify a non-canonical autophagy pathway and ER-shaping proteins as critical host determinants of DMV formation and functional coordination.

Using high-content siRNA screening targeting 48 autophagy-related genes, we uncovered 19 host dependency factors and 2 restriction factors that modulate SARS-CoV-2 infection. Among these LC3C and the ATG4D protease, able to delipidate LC3, emerged as key regulators. Functional validation across multiple cell lines and β-coronaviruses (SARS-CoV-2 and HCoV-OC43) revealed that ATG4D depletion impairs viral replication and infectivity, independent of canonical autophagy flux. Notably, ATG7-mediated LC3 lipidation is dispensable, suggesting that SARS-CoV-2 preferentially exploits unlipidated LC3C maintained by ATG4D. Reconstitution experiments with phosphomutant LC3C variants demonstrate that the non-phosphorylated, ATG4D-accessible form of LC3C supports viral replication, whereas the phosphomimetic form does not. These findings indicate that SARS-CoV-2 hijacks recycled LC3C to facilitate viral replication, bypassing the degradative autophagy pathway.

Parallel investigations into ER-shaping proteins reveal that atlastin-2 (ATL2), but not ATL3, is essential for provide DMV structural integrity and coordinate viral replication and assembly. ATL2 localises to three-way ER junctions and interacts with viral proteins nsp3 and nsp4. ATL2 knockout leads to the formation of smaller, open DMVs and Spike protein retention in the ER, impairing virion assembly and subsequently infectivity. Reconstitution of the ATL2B, but not ATL2A, isoform restores viral infectivity, underscoring isoform-specific functionality.

Together, these findings delineate a novel host-driven mechanism for DMV formation and organisation involving non-canonical autophagy and ER membrane dynamics proteins. This work provides mechanistic insight into host–virus interactions and identifies potential therapeutic targets for disrupting coronavirus replication.

Table of Contents

Acknowledgments

The work presented in this thesis was supported by a PhD Fellowship from the University of Federico II. in Naples and the Scuola Superiore Meridionale (SSM). The experiments were performed in the laboratory of Prof. Mirko Cortese in the Telethon Institute of Genetics and Medicine (TIGEM) and in the laboratory of Prof. Lina Herhaus in Helmholtz Institute for Infectious Diseases (HZI), under their mentorship.

I would like to thank Professor Paolo Grumati and Professor Carmine Settembre for kindly provided materials. I also gratefully acknowledge the scientific and technical support of TIGEM HCS and Microscopy facilities that made this work possible.

Dedication

To my mentor Mirko, for his guidance throughout these years.

To Lucia, for her help with the project, and to my group, for their support.

To my family, for their unwavering love; to all those who kept me going; and to everyone who strives to make science a little clearer and the world a little kinder.

Thank you.

“Begin at the beginning," the King said, very gravely, "and go on till you come to the end: then stop.”

— Lewis Carroll, Alice in Wonderland

1 Introduction

Over the past 25 years, human coronaviruses have transitioned from causing predominantly mild upper respiratory tract infections—such as those associated with HCoV-NL63, HCoV-229E, and HCoV-OC43—to triggering three major outbreaks of highly pathogenic viruses: the 2002 outbreak of Severe Acute Respiratory Syndrome Coronavirus (SARS-CoV), the 2012 Middle East Respiratory Syndrome Coronavirus (MERS-CoV), and the most recent global pandemic caused by SARS-CoV-2 in 2020. The COVID-19 pandemic alone has led to more than 704 million confirmed cases and over seven million deaths worldwide. This unprecedented event underscored the critical importance of studying the life cycle of positive-sense single-stranded RNA (+ssRNA) viruses, highlighting the need for a deep understanding of how these viruses interact with host cells to anticipate and mitigate future outbreaks[1].

This dissertation focuses on coronavirus–host interactions, with the aim of identifying key cellular factors involved in viral replication, assembly, and egress. The thesis is divided into two main sections, each exploring the role of a major host endomembrane system. The first part explores the autophagic pathway, which generates intracellular structures that morphologically closely resemble coronavirus-induced viral replication organelles (vROs). The second part focuses on the role of endoplasmic reticulum (ER)–shaping proteins, particularly atlastins, in viral progression, given the ER's leading role as the membrane source for vRO biogenesis.

1.1 Coronaviruses

1.1.1 Classification

Coronaviruses are enveloped viruses with non-segmented positive-sense single-stranded RNA genome. They belong to the *Coronaviridae* family, *Orthocoronavirinae* subfamily within the order *Nidovirales* (International Committee on Taxonomy of Viruses). The family is divided into four genera based on phylogenetic relationships and genome structure: *Alphacoronavirus*, *Betacoronavirus*, *Gammacoronavirus*, and *Deltacoronavirus*.

While *Alpha* and *Betacoronaviruses* primarily infect mammalian hosts, including humans and bats, and are associated with mild to severe respiratory and gastrointestinal diseases, the

Gammacoronaviruses and *Deltacoronaviruses* predominantly infect birds, although they can occasionally cross species barriers to infect mammals[2].

Among human-infecting coronaviruses, four are considered endemic and are typically associated with mild, seasonal upper respiratory tract infections: HCoV-229E and HCoV-NL63 (*Alphacoronaviruses*), and HCoV-OC43 and HCoV-HKU1 (*Betacoronaviruses*). Of these, HCoV-OC43 is particularly notable as it is believed to have crossed into humans from bovine coronavirus (BCoV) in the late 19th century, potentially coinciding with a respiratory pandemic in 1889[3,4]. This zoonotic jump illustrates how coronaviruses can adapt to human hosts and circulate endemically over time. Despite causing only mild illness today, OC43 and related strains underscore the evolutionary potential of Betacoronaviruses to acquire increased pathogenicity.

In fact, the most clinically significant high-risk human pathogens belong to the genus *Betacoronavirus*, including Severe Acute Respiratory Syndrome Coronavirus (SARS-CoV), Middle East Respiratory Syndrome Coronavirus (MERS-CoV), and Severe Acute Respiratory Syndrome Coronavirus 2 (SARS-CoV-2). SARS-CoV-2, the aetiological agent of COVID-19. Notably, it is genetically closest to the bat-derived coronaviruses with 96% identity at the whole-genome level to a bat coronavirus, reflecting its likely zoonotic origin[5–7].

1.1.2 Virion structure and genome organisation

Coronavirus virions are spherical particles ranging in diameter from approximately 80 to 160 nm[2]. A hallmark feature of the virion is its crown-like appearance under electron microscopy, formed by homotrimers of the spike (S) glycoprotein protruding from the viral envelope. This structure, reminiscent of the solar corona, is the origin of the family's name[8]. The virion is composed of four main structural proteins: spike (S), membrane (M), envelope (E), and nucleocapsid (N)[9].

The S protein, the largest of the structural proteins (~150 kDa), is heavily glycosylated and consists of an ectodomain, a single-pass transmembrane anchor, and a short intracellular tail. The ectodomain comprises two functional subunits: S1, which mediates receptor binding, and S2, which facilitates membrane fusion[10]. The most abundant structural protein is the M protein (~25–30 kDa), which spans the membrane three times and contains a glycosylated N-terminal ectodomain and C-terminal endodomain. M's ectodomain probably plays a role in determining the shape of the virion and in coordinating virus assembly. The E

protein (~8–12 kDa) is the smallest and least abundant structural component. Despite its low abundance, it plays key roles in virion morphogenesis and budding. Its N-terminus faces the exterior of the virion, while the C-terminal endodomain harbours ion channel activity (viroporin function). Beneath the envelope lies the helically symmetrical nucleocapsid encapsulating the viral genome, formed by the N protein (~50 kDa). The N protein is highly phosphorylated and contains two RNA-binding domains (N-terminal and C-terminal), which bind the viral genome in a beads-on-a-string manner and ensure thus the successful genome packaging into newly assembled virions. These interactions are further stabilised by interactions with the M protein and the non-structural protein 3 (nsp3).

Together with the other members of the order *Nidovirales*, the coronaviruses genome is notably large, spanning from 27 to 32 kbp. It is capped at the 5′ end and polyadenylated at the 3′ end [11,12]. Majority of the genome encodes the large replicase gene, which translates from two open reading frames (ORF), ORF1a and ORF1b, to pp1a/pp1ab polyprotein. The −1 ribosome frameshift happens right upstream of the ORF1a stop codon, which allows continued translation of ORF1b, yielding a larger polypeptide. After translation, the polyproteins are cleaved into sixteen non-structural proteins (nsp), responsible for the formation of the replication-transcription complex (RTC) and driving viral genome replication and subgenomic mRNA (sgRNA) synthesis. Finally, toward the 3' polyadenylated end lie the structural genes for S, E, M and N proteins along with a variable number of accessory genes.

1.1.3 HCoV-OC43

First identified in 1967, Human Coronavirus OC43 (HCoV-OC43) is the coronavirus most associated with recurrent common-cold-causing infections. It is estimated as the cause of 10–15% of acute respiratory diseases of both upper respiratory tract infections as well as bronchitis and pneumonia across all age groups[13–15]. Despite its early discovery, genomic studies of HCoV-OC43 remained scarce until the first complete genomes were reported in 2004, revealing considerable genetic diversity and evolutionary pattern[3]. Molecular epidemiological investigations have identified at least three distinct phylogenetic clusters of HCoV-OC43, which further differentiate into four genotypes (A through D), with genotype D emerging as a result of natural recombination events between genotypes B and C. Molecular clock analysis dates the most recent common ancestor of all genotypes to the 1950s, suggesting relatively recent evolutionary divergence[14,16].

The molecular architecture of HCoV-OC43 reveals a putative receptor binding domain (amino acid positions 339 to 549) on the S protein facilitating viral attachment to sialic acid receptors on host cells and determining thus different tropism from later emerged CoVs[15,17]. HCoV-OC43 undergone remarkable evolutionary path, where the earliest genotype A, represented by the ATCC and Paris laboratory strains isolated approximately five decades ago, appears to have been replaced by newer genotypes in contemporary infections. Circulating strains analysis show a clear succession of dominant genotypes: genotype B predominated in 2004, genotype C circulated from 2004 to 2006, and the recombinant genotype D emerged in 2004 and became the exclusive genotype identified between 2008 and 2011[14]. Moreover, genotype D HCoV-OC43 infections were disproportionately associated with pneumonia cases in elderly patients, and this progression suggests ongoing viral adaptation to hosts through both gradual mutation and recombination events, potentially resulting in enhanced virulence or altered tissue tropism[18]. In the last decade, five more additional genotypes, namely E, F, G, H, and I were described, pointing to the adaptive potential of HCoV-OC43 and the importance of continued molecular surveillance to monitor changes in Coronaviruses epidemiology and pathogenicity[16,19–21,18].

1.1.4 SARS-CoV

Severe Acute Respiratory Syndrome Coronavirus (SARS-CoV) belonging to the *Betacoronavirus* genus, subgenus *Sarbecovirus*, caused the first documented outbreak of a highly pathogenic human coronavirus. The virion containing ~29.7 kb long genome used the angiotensin-converting enzyme 2 (ACE2) as its host receptor, with viral entry facilitated by the S glycoprotein and promoted by proteolytic activation of the S by host proteases such as TMPRSS2[22,23]. SARS-CoV emerged for the first time in November 2002 in Guangdong Province, China, where it probably spilled over from a bat reservoir[24]. Thanks to easy transmission, via direct contact and liquid droplets, by March 2003 it spread internationally to Hong Kong, Beijing, Singapore, Vietnam, and even EU countries as France or Germany, resulting in more than 8000 confirmed cases and 700 deaths, with a case fatality rate of approximately 9.6% (WHO,2015)[25](https://www.who.int/publications/m/item/summary-of-probable-sars-cases-with-onset-of-illness-from-1-november-2002-to-31-july-2003). Unlike previously known human coronaviruses that typically caused mild upper respiratory illnesses, SARS-CoV was markedly more virulent. In severe cases, the disease advanced to acute

respiratory distress syndrome (ARDS), often requiring intensive care support[26]. The SARS epidemic thus underscored the need for rapid diagnostic development, global surveillance networks, and transparent reporting in infectious disease outbreaks. Although the virus was ultimately contained through non-pharmaceutical interventions, thanks to its ~5 days delayed peak in viral load in the upper respiratory tract, the episode highlighted the potential for coronaviruses to cause global health crises[26,27] —a warning realized another two times in the years to come, ultimately with the 2020 COVID-19 pandemic.

1.1.5 MERS

A decade after the SARS-CoV outbreak, a novel and highly pathogenic coronavirus—Middle East Respiratory Syndrome Coronavirus (MERS-CoV)—was identified in 2012 in Jeddah, Saudi Arabia, from a 60-year-old patient who died of severe pneumonia and multiorgan failure[28]. MERS-CoV rapidly raised global concern due to its high case fatality rate of approximately 36% and potential for international spread (WHO, 2025). Primary cases were reported in Middle Eastern countries such as Jordan, Qatar, Saudi Arabia, and the United Arab Emirates, with subsequent travel-associated cases confirmed in Europe and North Africa. As of the latest WHO update in March 2025, 2,618 laboratory-confirmed cases and 945 deaths have been reported globally (WHO, 2025).

Clinically, MERS-CoV infection manifests across a broad spectrum—from asymptomatic or mildly symptomatic cases (e.g., low-grade fever, cough, sore throat, and myalgia) to severe pneumonia, ARDS, septic shock, multiorgan dysfunction, and acute kidney injury. Severe disease is predominantly observed in older adults and individuals with comorbidities, such as diabetes, cardiovascular diseases, or immunosuppressive conditions[29]. In contrast to SARS-CoV, MERS-CoV exhibits limited human-to-human transmission. Documented transmission has primarily occurred among close contacts—within households or in healthcare settings involving patients and healthcare workers – and is attributed to the virus's cellular tropism; MERS-CoV utilizes dipeptidyl peptidase-4 (DPP4/CD26) as its entry receptor, which is expressed predominantly in the lower respiratory tract epithelium but is absent or minimally expressed in the upper airways[30,31]. Consequently, MERS-CoV replication is largely confined to the lower respiratory tract, resulting in low viral RNA loads in nasopharyngeal samples, which likely restricts transmissibility through casual contact[32].

Even though MERS-CoV is currently an endemic, low-risk threat, its zoonotic potential can lead to further mutations and outbreaks.

1.1.6 SARS-CoV-2

With even shorter period between the last and new outbreak, in November 2019, a novel coronavirus, later named Severe Acute Respiratory Syndrome Coronavirus 2 (SARS-CoV-2), was identified in Wuhan, China, as the causative agent of a cluster of pneumonia cases. Epidemiological investigations linked early cases to the Wuhan Huanan Seafood Wholesale Market suggesting, similarly with other high-pathogenic coronaviruses, a zoonotic origin. Environmental samples from the market tested positive for SARS-CoV-2, particularly in areas where live wild animals were sold, including species such as raccoon dogs and civets, which are known to be susceptible to coronaviruses. The virus was isolated on January 9, 2020, and its 29,9 kbp long genome was sequenced and shared globally by Chinese authorities on January 12 (https://www.who.int/emergencies/disease-outbreak-news/item/2020-DON233). These findings confirmed that the virus was a positive-sense RNA virus belonging to the *Coronaviridae* family, specifically a novel *Betacoronavirus* (subgroup B) previously unknown to humans. Early genomic analysis revealed a high degree of sequence similarity to SARS-CoV (79.6% genome identity) and only low sequence similarity with MERS (50%)[7,33,34]. Phylogenetic analyses indicated the presence of two distinct viral lineages (A and B) circulating concurrently, implying multiple spillover events from animals to humans[35]. The virus rapidly spread globally, leading the World Health Organisation (WHO) to declare a Public Health Emergency of International Concern on January 30, 2020, and subsequently a pandemic on March 11, 2020. Since its emergence, SARS-CoV-2 has undergone genetic evolution, leading to the emergence of several Variants of Concern (VOCs) characterised by mutations that affect transmissibility, virulence, and immune escape, which further necessitates ongoing surveillance and adaptation of public health strategies. As of September 2025, SARS-CoV-2 has resulted in over 778 million confirmed cases of COVID-19 and more than seven million deaths worldwide (WHO, 2025). The pandemic has had profound impacts on global health systems, economies, and societies, making it one of the most significant public health crises in modern history, underscoring once more the critical need for understanding the coronavirus's biology and pathogenesis.

1.1.6.1 Replication cycle

SARS-CoV-2 initiates infection by binding its S glycoprotein to the host cell receptor ACE2[23]. This interaction is facilitated by the host serine protease TMPRSS2, which cleaves the S protein, enabling fusion of the viral envelope with the cell membrane[36]. Alternatively, the virus can enter via endocytosis, where endosomal acidification and cathepsin-mediated cleavage activate the S protein[37](Figure 1).

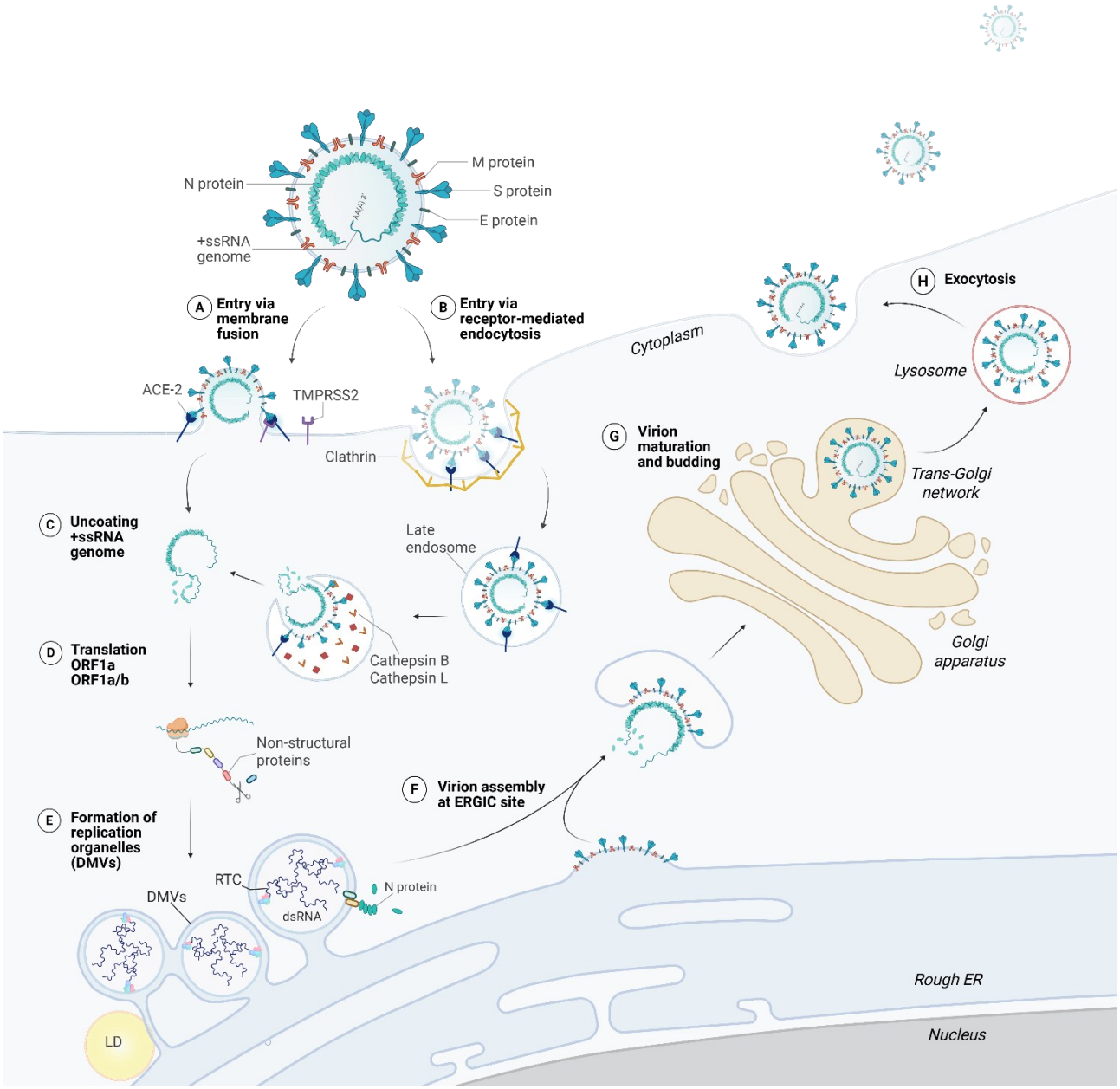

Figure 1: Schematic representation of SARS-CoV-2 life cycle. SARS-CoV-2 attaches to ACE2 and TMPRSS2 membrane receptors and enters the cell by (**A**) membrane fusion or (**B**) receptor-mediated endocytosis. (**C**, **D**) Released viral +ssRNA genome serves directly as mRNA for viral polyproteins ORF1a and ORF1ab translation.

(**E**) The polyproteins are cleaved into 16 non-structural proteins to subsequently assemble the double-membrane vesicles (DMVs) and replication transcription complex (RTC) allowing synthesis of new genomes and sub-genomic RNAs coding for structural and accessory proteins. (**F**) Structural proteins - the membrane, envelope and spike protein – are maturated via the secretory compartment trafficking and accumulate at the membrane of the ER—Golgi intermediate compartment (ERGIC), where they assemble together with nucleocapsid and dsRNA genomes into new viral progeny. (**G**) The maturation and budding of new virions occur in the Golgi apparatus and trans-Golgi network. (**H**) Newly produced progeny finally exits cells through the secretory pathway or exocytosis. Adapted from Marano, V., Vlachová, Š., Tiano, S.M.L. *et al.* [38]

Following entry, the viral envelope merges with the host membrane, releasing the viral RNA into the cytoplasm, where it serves directly as messenger RNA (mRNA)[39]. The 5′ two-thirds of the genome contains two large open reading frames, ORF1a and ORF1ab, which are translated into polyproteins pp1a and pp1ab (Figure 2). The production of pp1ab involves a programmed -1 ribosomal frameshift at a slippery sequence (UUUAAAC) followed by a pseudoknot structure, allowing the ribosome to bypass the ORF1a stop codon. The efficiency of this frameshifting event is regulated by a 5′ attenuation loop located upstream of the slippery sequence, as well as by interactions between the translating ribosome and the emerging nascent polypeptide chain[40]. The polyproteins pp1a and pp1ab are cleaved by the nsp3 and nsp5 viral proteases: the papain-like protease (PL^pro) in nsp3 and the main protease (M^pro or 3CL^pro) within nsp5[41,42]. This cleavage yields 16 non-structural proteins (nsps), which assemble into the RTC in newly formed vROs[43].

The RTC holoenzyme includes the RNA-dependent RNA polymerase (RdRp) nsp12, nsp13 (helicase), and the nsp7, nsp8 and nsp9 cofactors. Other factors such nsp10, nsp14, nsp16 are factors essential for viral RNA synthesis[44,45]. Identically to SARS-CoV, the nsp3, nsp4 and nsp6 of SARS-CoV-2 induce the rearrangement of host cellular membranes to form the vROs, specifically double-membrane vesicles (DMVs), which are derived from ER and serve as sites for viral RNA synthesis[46–48]. DMVs are the primary site for RNA synthesis, but other virus-induced organelles, like convoluted membranes and single-membrane vesicles, have also been observed[49–51]. During replication, a full-length negative-sense RNA strand template is synthesised from the genomic positive-sense RNA, transiently forming a double-stranded RNA (dsRNA) intermediate[52]. This template serves to produce new +ss genomic RNA and a set of sgRNAs, through a process called discontinuous transcription, in which a common 5′ leader sequence (~70 bp) is fused to downstream body sequences of the genome[39]. The

common leader sequence is present only once at the 5′ terminus of genome, suggesting non-contiguous sequence fusion, where the leader sequence fuses with the 5′ end of each sgRNA coding sequence, called the body. Based on the currently most accepted model, the leader-to-body fusion occurs during -ssRNA transcription at short motifs called transcription-regulatory sequences (TRS) positioned directly adjacent to ORFs[53]. Practically the RdRP pauses upon meeting TRS in the body and shifts the template to the TRS in the leader[39,42].

The newly synthesised sgRNA and genomic RNA are subsequently transported outside the DMV through the nsp3-nsp4-formed molecular pore[54,48,55]. The structural, non-structural and supposedly eight accessory proteins (3a, 3c, 6, 7a, 7b, 8, 9b and 10) are translated on ribosomes associated with the rough ER and transported to the ER-Golgi intermediate compartment (ERGIC) GeneBank: NC_045512.2). The newly synthesised genomic RNA associates with the N protein to form ribonucleoprotein complexes, which are then directed to the ERGIC to assemble with S, E, and M proteins into new viral progeny[56]. While it is known that N, S, M and E alone can compose a virus-like particle, the precise mechanisms establishing the balance between sgRNA and genomic RNA, as well as the relative abundance of sgRNAs, and structural proteins, remain unclear. It is presumable that the precise regulation of assembly process is required as the stoichiometry of individual components in the virion can ultimately affect viral infectivity[57–59]. The M, E, and S mRNAs share identical 5′ and 3′ UTRs, which interact with proteins involved in mRNA trafficking and translation regulation. As a result, their translation is likely to occur at the same or nearby ER sites. This spatial coordination could facilitate their co-sorting into the same COP-II vesicles route to the ERGIC.[60–62].

Finally, the mature virions are transported in vesicles of the conventional secretory pathway from trans-Golgi to the cell surface and released via exocytosis, or alternatively can be released through lysosome-mediated exocytosis in multi-vesicular bodies (MVB)[50,63–66].

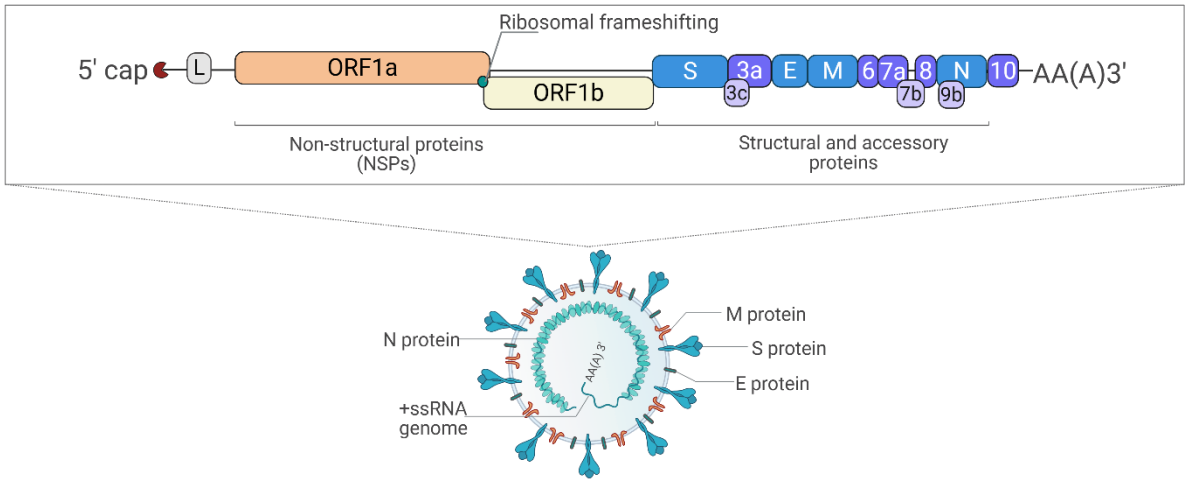

Figure 2: Scheme of SARS-CoV-2 genome and virion structure. Adapted from Marano, V., Vlachová, Š., Tiano, S.M.L. *et al.*[38]

1.1.6.2 Double membrane vesicles

As SARS-CoV-2 replicates its large genome in the cytoplasm, it extensively reshapes the infected cells by inducing an elaborate reticulovesicular network of DMVs, acting as central hubs for viral RNA replication[49,50,67]. The lumen of the DMV provides a shielded environment for optimal virus replication allowing higher spatial concentration of viral enzymes, metabolites and overall macromolecules required for RNA synthesis. Additionally, replication organelles likely protect double-stranded RNA intermediates from host immune sensors as RIG-I or MDA5. Recent studies reveal that host factors such as fragile X–related (FXR) proteins (FXR1/FXR2/FMR1) are essential for DMV clustering via liquid–liquid phase separation, a process hijacked by SARS-CoV-2. FXR proteins are recruited to DMV sites via interaction with nsp3, and their phase separation properties help DMV clustering, facilitating efficient translation and enhancing replication efficiency[68]. Furthermore, DMVs physically separate the RTC from sites of translation and virion assembly, enabling spatiotemporal coordination of distinct stages in the viral life cycle and preventing functional interference among them[49,50,54].

In SARS-CoV-2-infected cells, DMVs typically range from 100 to 300 nm in diameter and are derived from the ER membranes[50,51]. Consistently with the ER origins, studies reveal that ER shaping reticulon proteins (RTN), RTN 3 and 4 are hijacked by SARS-CoV-2 non-structural proteins to enhance the DMVs biogenesis[69]. Current models suggest that the ER cisternae membranes are reshaped to form DMVs in a process predominantly orchestrated by the

nsp3 and nsp4. These two nsps compose the minimal core machinery required for membrane curvature and vesicle closure as their co-expression alone is sufficient to induce DMV formation, as demonstrated in both SARS-CoV and SARS-CoV-2 systems[46,48,50,54]. DMVs are often clustered and connected via a nsp6-mediated network of closely opposed ER membrane continuities with a limited lumen, known as "zippered ER," which serves as a scaffold for DMV formation[47,51,50]. The biogenesis of DMVs is primarily driven by three SARS-CoV-2 non-structural proteins—nsp3, nsp4, and nsp6—each of which contains multiple transmembrane domains. The nsp3 localizes predominantly to the outer DMV membrane, while nsp4 is enriched on the inner leaflet, and their interaction is essential for the double-membrane architecture. Although nsp6 is not strictly required for DMV formation, it plays a key role in shaping the DMV network and its spatial organisation. Nsp6 mediates the tethering of DMVs to the ER and possibly to lipid droplets, functional membrane contacts that facilitate lipid exchange and membrane expansion[47]. Lipid droplets, which are known to be depleted during SARS-CoV-2 infection, are believed to contribute lipids for membrane biogenesis[70]. Additionally, the depletion of lipid droplets during infection underscores the high metabolic demand imposed by DMV formation[71–73].

DMVs, whose outer membrane is often studded with ribosomes, are present in infected cells as soon as 2 h post-infection[50]. The long-standing conundrum in +ssRNA virology: how membrane-shielded RNA products access the cytosolic translation machinery without compromising DMV integrity, was solved by Wolff *et al*., who used *in situ* cryo-ET analysis of murine hepatitis virus (MHV) infected cells identifying a proteinaceous pore spanning the virus-induced DMV membranes[54]. Thus, DMVs are not sealed structures but are connected to the cytosol via molecular pores embedded in their membranes and composed mainly of nsp3 and nsp4. These pores are believed to mediate the export of newly synthesised positive-strand genomic and subgenomic RNAs from the DMV lumen to the cytoplasm, where translation and virion assembly occur[49,50,67].

In recent years, also the SARS-CoV-2 DMV-spanning pore was described, thanks to cryo-electron tomography (cryo-ET) and sub-tomogram averaging. The method used by Zimmermann *et al*. and subsequently Huang *et al*. allows observation of the DMVs pore in the native cellular environment under low biosafety conditions as nsp3-nsp4 transfection-induced DMVs or low pathogenicity CoV models were used[48,74]. The double-membrane-

spanning pores consist of nsp3 and nsp4 as their minimal constituents and bear remarkable similarity to the nuclear pore complex[48,74]. Nsp4 interacts with nsp3 on the cytoplasmic side and because nsp4 forms the lumen-facing component of the pore complex, it is a likely candidate for interacting with the replicase machinery. Experimental data indicate that nsp4 interacts with nsp8 either alone or as part of a nsp7-nsp8 complex, supporting structural predictions of a sixfold symmetric nsp4-nsp8 assembly. However, it remains unclear whether the connection between the replicase and the pore is mediated solely by nsp8 or through a broader molecular interface that may also involve RNA[55].

The nsp3-nsp4 pore complex, resolved at 4.2 Å resolution, exhibits a striking architecture organized with intriguing stoichiometry and topology into 4 concentric stacked hexamer rings, comprising 12 copies each of nsp3 and nsp4. The transmembrane domains of nsps intertwine to create a high local curvature at the double-membrane junction, resulting in coupling of double-membrane reshaping with pore formation. The ectodomains form extensive interactions arranged in a pseudo-12-fold symmetry, encircling the pore complex from within the inter-membrane space[74]. At the centre, a narrow ring of positively charged arginine residues of nsp4 is thought to coordinate nascent viral RNA translocation from the DMVs lumen—an essential step in viral replication[55,74]. Structural modelling further indicates that this constriction is sufficient to accommodate ssRNA, but it is too narrow to permit the passage of dsRNA[55].

The formation of DMVs is partially dependent on the autophagy-related machinery, although canonical autophagosome-lysosome-mediated degradation is dispensable[73,75]. Rather than inducing complete autophagic flux, the virus appears to co-opt selected components, such as ER shaping proteins and lipid transfer proteins, to stabilise DMV structures[71]. DMVs' biogenesis and maintenance are tightly linked to host lipid metabolism, with proteins such as VMP1 and TMEM41B being essential for efficient viral replication due to their roles in membrane morphogenesis and lipid homeostasis[72].

Despite considerable advances in our understanding of DMV architecture and composition, many aspects of their biogenesis remain unresolved. The precise molecular mechanism by which nsp3–4–6 orchestrates membrane curvature, how DMV pore selectivity is regulated, and how interactions with host lipid metabolism are spatially and temporally coordinated are subjects of ongoing investigations.

1.1.6.3 Viral proteins

The SARS-CoV-2 virus, like other viruses, is an obligate pathogen that relies on the host cell's translation machinery for viral gene expression. Viral proteins promote mechanisms that inhibit host mRNA processes while accelerating viral disease progression, thereby driving viral pathogenicity, immune evasion and virus-host interactions[76–80]. SARS-CoV-2 is encoding for at least 26 viral proteins, comprising 4 structural, 16 non-structural and 8 accessory proteins.

Significant progress has been made in elucidating how viral proteins function and which sort of post-translational modifications (PTMs) they undergo, providing essential knowledge about COVID-19 disease mechanisms and enlightening the difference in virulence and pathogenicity compared to related coronaviruses[81,82]. The most common PTMs observed in SARS-CoV-2 proteins include glycosylation, phosphorylation, and acylation[82].

Glycosylation, particularly prominent on the S protein, plays a crucial role in SARS-CoV-2 pathogenicity and immune evasion. N- and O-linked glycosylation sites on the S protein surface form a "glycan shield," which masks immunogenic epitopes from host antibodies while preserving the protein's ability to bind the ACE2 receptor[83,84]. Phosphorylation, which is primarily targeting N protein, enhances the N's selective binding to viral RNA, promoting replication and transcription processes and increasing the viral load within the host by optimising the efficiency of viral genome packaging[82,85]. The phosphorylation status of viral proteins dynamically changes during infection, allowing the virus to adapt to different cellular environments and stages of the infection cycle[85]. This adaptability contributes to the virus's ability to establish persistent infection and evade host defence mechanisms. Succinylation of the N and M proteins has been observed to synergistically affect virus particle assembly[86]. Additionally, the accumulation of mutations in SARS-CoV-2 variants has led to altered PTM profiles, with implications for viral fitness, transmissibility, and immune escape relative to the ancestral Wuhan strain[87].

Unlike host proteins, whose degradation is tightly regulated by cellular quality control systems such as the ubiquitin–proteasome system and autophagy, viral proteins often exploit or evade these pathways to extend their functional lifespan or avoid degradation[88,89]. A comprehensive study profiling 25 viral proteins revealed that 18 are unstable, with half-lives ranging from 0.4 to 8 hours, including nsp1 (1.57 hours), E (3.92 hours), and ORF8 (0.48 hours)[88], as shorter

half-lives are better suited to temporally regulated functions such as host translational shutoff and RNA proofreading[88]. These unstable proteins are predominantly degraded via the ubiquitin-proteasome pathway. In contrast, seven proteins-nsp2, nsp5, nsp10, nsp15, S, M, and N -demonstrate greater half-life, allowing fast accumulation and persistence, but also eliciting stronger antibody responses due to their prolonged presence. This stability is thought to be facilitated by phosphorylation-dependent shielding from host proteolytic machinery and incorporation into phase-separated condensates that resist degradation. Viral proteins like ORF3a and ORF8 have been shown to interact with components of the ER-associated degradation (ERAD) pathway, which may either promote degradation or subvert it to regulate host immune signalling[90,91].

1.1.6.3.1 Structural proteins

1.1.6.3.1.1 Spike

Entry of SARS-CoV-2 into host cells is mediated by the S glycoprotein, a 1273-amino-acid-long protein composed of two subunits. The S1 subunit binds to the host receptor ACE2 via its receptor-binding domain (RBD), facilitating viral attachment, while the S2 subunit drives membrane fusion. For this process to occur, the S protein must be primed by host furin and TMPRSS2 proteases. Furin cleaves S at the multi-basic arginine residues-rich S1/S2 site and TMPRSS2 cleaves the S2′ site, thereby enabling the fusion of viral and cellular membranes and allowing subsequent viral replication[7,83,92,93]. The S protein's pivotal role in the virus ability to infect host cells is making it a critical target for therapeutic and vaccine development[23,93].

The spike protein is characterised by its complex structure, which includes multiple glycosylation sites that modulate its immunogenicity and stability, thereby influencing the host immune response[94]. The S1 subunit, residues 14–685, contains the N-terminal domain (NTD, residues 14–304) and RBD (residues 319–541)[95]. The S2 subunit, residues 686–1,273, includes the fusion peptide, heptad repeats, transmembrane domain, and cytoplasmic tail[95]. The trafficking of S is quite complex, after the translation on ER it acquires multiple mannosylations, as shown by its sensitivity to Endoglycosidase H (EndoH) treatment, which correspond to a 170 kDa trimeric protein. Subsequently the high-mannose S converts to complex type N-glycans enriched S (~180kDa) in the *cis* to *medial* Golgi[96]. The time-dependent increase of complex N-glycan-rich S protein signal abundance is counter-

parted by the progressive decrease of the EndoH-sensitive S, which corresponds to the efficient maturation of spike dependent on the ER-Golgi trafficking.

Recent studies have highlighted the importance of specific mutations within the spike protein, such as those found in variants of concern, which can enhance transmissibility and evade neutralising antibodies[84,87].

1.1.6.3.1.2 Envelope

The E protein is the smallest SARS-CoV-2 protein with length of 75 amino acids, corresponding to 10kDa protein size, it shares 94.74% identity to SARS-CoV's E. It consists of the hydrophobic α-helical transmembrane domain (residues 12-39) and amphiphilic α-helices H2 and H3, connected by flexible linkers at the membrane surface[97,98]. The membrane single-spanning E protein's N-terminus is exposed into the ER lumen and translocate across the membrane, while the C-terminus is exposed to the cytoplasmic side[99]. The E can sense and induce membrane curvature in its monomeric as well as polymeric form, suggesting its role in virion budding. Moreover, in its pentameric ion channel form E protein acts as a viroporin through its C-terminal post-synaptic density protein-95/discs Large/zonula occludens-1 (PDZ) domain binding motif, affecting viral assembly, virulence and pathogenicity[99–101]. To perform its main function in virus assembly, E protein mainly localises to the ERGIC, where it cooperates with M and other structural proteins[99]. Boson *et al*. showed that E can slow down the cell secretory pathway and indirectly affect the Spike maturation [102]. The E has a very short lifespan, shown by colocalization with Erp72 ER marker, but lacking a typical ER-type pattern distribution[88,96].

Structural conformation and oligomerisation of E is controlled by PTMs. E is, in contrast to S and M, poor in *N*-glycosylation sites, and it is mostly dependent on palmitoylation[96]. Specifically, the palmitoylation of cysteines Cys40, Cys43, and Cys44 affects H2 helix and the H3 helix is influenced by single glycosylation of Asn66[97,101].

1.1.6.3.1.3 Membrane

The membrane protein is 222 amino acids and 50.2 kDa long transmembrane dimeric glycoprotein, and is the most abundant structural protein of SARS-CoV-2 [103,104]. After synthesis on ER, M protein mainly localises to the ERGIC [96,105]. M is not only the most abundant viral structural protein, but also an indispensable part of the virion as it is, together

with N or S protein, the minimal required component for virus like particles formation[58,106]. The virion assembly is achieved through M homotypic and heterotypic (with S, E and N) interactions which initiate membrane curvature and are thus essential for virion formation. The M interactions with N and RNA are mediated through the positively charged C-terminal intra-virion domain[105]. The M transmembrane helices are interacting with C-terminal retrieval motif of S protein in its cytoplasmic tail, and this interaction is important for the retention of S in the ERGIC compartment. Furthermore, the S-M interaction is also crucial for S protein maturation, particularly glycosylation, which S undergoes via its Golgi trafficking[107].

The M protein exists either in a mushroom-shaped dimer form, composed of two highly hydrophobic transmembrane domain three-helix bundles and two positively charged intra-virion domains, or in a higher order multimeric form[105]. The dimeric form is stabilised by several residues (W20, W58, P59, W92, L93 Y95, and F96) spread along the three transmembrane domains of each monomer[108]. Both - dimeric and higher order multimeric, forms are important for the correct virion assembly. Zhang *et al*. showed that M protein oligomers organised in tandem are capable of inducing mild curvature of the membrane, likely contributing to the round virion particle shape[105]. This finding was recently confirmed by another study, combining cryo-EM and atomic force microscopy (AFM), revealing a lipid membrane thinning by 0.5 nm in the vicinity of side-by-side M dimer incorporation to membrane resulting in line tension, potentially driving the structural proteins aggregation and subsequent shaping the new virions[104].

1.1.6.3.1.4 Nucleocapsid

N protein is a flexible and multivalent RNA-binding 419 amino acids long protein essential for viral genome packaging and assembly[109,110]. Structurally, it consists of two main functional domains—the N-terminal domain (NTD), which binds RNA, and the C-terminal domain (CTD), responsible for dimerization and additional RNA binding—connected by a serine/arginine-rich flexible intrinsically disordered linker. The central flexible linker is complemented by other two inartistically disordered regions (IDRs) that facilitate multivalent interactions with RNA and other proteins such as nsp3, contributing to its flexibility and functional diversity[109]. In particular, the N-nsp3 interaction was shown as crucial for N contact with the RTC and subsequent RNA binding[110]. Recent studies using single-molecule spectroscopy and simulations reveal that SARS-CoV-2 N, similarly as other coronaviruses'

N proteins, thanks to its IDRs and RBD, undergoes liquid-liquid phase separation with RNA *in vitro* based on pH, salt content and RNA concentration[111]. This phase separation ability is believed to drive viral RNA compaction and nucleocapsid formation[109].

Interestingly, Nucleoprotein possesses the highest amount of phosphosites among SARS-CoV-2 proteins. There are two phosphorylation sites-rich clusters localised at the N-terminal region (S21–S33) and linker region after the RBD (Y172-S202)[87]. The mutations of N regulatory regions in variants of concerns, particularly Delta and Omicron, revealed importance of this protein in the adaptation of SARS-CoV-2 to humans[112].

1.1.6.3.1.5 Non-structural proteins

Nsp1 is a 180 amino acid viral protein of SARS-CoV-2 that shares structural homology with other β-coronaviruses' nsp1, even if the sequence is highly variable. Nsp1 interacts with the mRNA entry tunnel of the 40 S ribosomal subunit through electrostatic and hydrophobic interactions of the C-terminus, while the N-terminus stabilises these bonds and ensures that only host genes translation is diminished via its interaction with SARS-CoV-2 5'UTR[113,114]. As the translational shutdown almost completely inhibits the host immune response, including interferon and proinflammatory cytokines production, and antiviral interferon-stimulated genes, nsp1 acts as a strong virulence and pathogenicity factor[113].

The 638 amino acids long nsp2 protein is associated with endosomal localisation. The three zinc fingers (ZnFs) in nsp2 N-terminal region, or the positively charged residues on the protein surface are believed to participate in viral replication, transcription, inhibition of host protein synthesis, mitochondrial biogenesis and immune evasion[80,115]. Nsp2 interacts with the host cap-binding protein eIF4E, an enzyme catalysing a key regulatory step in mRNA translation, supporting its role in manipulating host cellular machinery. However, the precise function of nsp2 protein remains unclear.[115]

On the other hand, much more is known about the two basic components of replication factories, which are nsp3 and nsp4. Nsp3, the longest protein in the viral genome and the largest coronaviral cysteine protease, composes of 1945 amino acid residues, and contains multiple functional domains including the papain-like protease (PLpro) domain, Ubiquitin-like domains (Ubl) and macrodomains (Mac)[115]. Nsp3 has at least 15 functional domains giving it a wide variety of functions, including proteolytic, deubiquitinating, and deISGylating

activity[116]. The evolutionary conserved first macrodomain, Mac1, hydrolyses mono-ADP-ribose from target proteins and fights the host-mediated antiviral ADP-ribosylation, making nsp3 a virulence factor[117]. Ubl1 domain is responsible for the nsp3 interaction with N[110]. The multifunctional nature of nsp3 makes it not only a critical component in the viral life cycle, but also a potential target for therapeutic intervention, with the example of SARS-unique domain being among one of the already proven druggable targets[118]. The PLpro domain is responsible for processing the N-terminal portion of the viral polyprotein pp1a thanks to recognition of the LXGG-motif and its hydrolysis into nsp1, nsp2, and nsp3[80]. Apart of polyprotein processing, nsp3 possesses many additional functions, such as DMVs biogenesis, RTC formation, component of the viral pore together with nsp4, responsible for viral RNAs trafficking between DMVs and cytoplasm, and innate immunity regulation[118]. Nsp3 Mac2-Mac3-DPUP-Ubl2 domains are critical for its oligomerization and integrity of the pore crown-like structure[48,55]. While nsp3 contains mainly cytosolic domains and only 2 transmembrane domains, nsp4 possesses 4 transmembrane domains and 2 ER lumen facing domains. The 500 amino acid residues long nsp4 protein is the other crucial building unit for DMVs and membrane pore biogenesis. It has been shown that nsp4 protein expression can induce ER membranes reshaping and activate unfolded protein response, and that the mutations in nsp4 protein of VOCs causing higher homodimerization are responsible for increased curvature of the ER membranes and promotion of DMVs formation[119,120].

The main protease (Mpro) nsp5 is a 306 amino acid residues long 3-cysteine-like protease (3Clpro). This protease is essential for viral replication as it is responsible for non-structural protein maturation via cleavage of the polyproteins pp1a and pp1b at 11 different sites, from NSP4-NSP16. Firstly, nsp5 catalytic function is activated after maturation of the protein through autocleavage and homodimerisation[115]. Then the protease activity alongside pp1a and pp1b begins thanks to the catalytic dyad of cysteine and histidine residues. There is high level of conservation along the cleavage sites, where the P1 position is strictly a conserved glycine and the P2 position show a preference of leucine, whereas the P1' position prefers smaller aliphatic residues[121].

Nsp6, a 294-amino acid protein containing eight transmembrane domains, forms homodimers and is localised in the endoplasmic reticulum (ER). These homodimers create

zippered ER structures that restrict the transport of ER protein with a bulky luminal part, while selectively permitting access to certain smaller membrane proteins and lipids[47]. In conjunction with nsp3 and nsp4, nsp6 is responsible for forming the DMVs. Furthermore, NSP6 orthologues in several coronaviruses, such as SARS-CoV, IBV, MHV or PRRSV, are responsible for omegasome formation and also LC3B relocalisation in infected cells[122]. Notably, nsp6 can also dampen the type I interferon production on several levels, such as supressing IRF3 or inducing nuclear factor kappa-light-chain-enhancer of activated B cells (NF-κB) by recruiting transforming growth factor beta-activated kinase 1 (TAK1)[115,123].

Nsp7 and nsp8 serve as cofactors forming the core of RTC, together with nsp12. Nsp12 is the catalytic subunit, and associates with nsp7 and nsp8 in a 1:1:2 ratio heterotetramer. Nsp7-nsp8 serve as processivity factors with priming activity ensuring efficient RNA synthesis and supporting nsp12 activity[115,124]. The nsp12 RNA template binding is functional only in the presence of both nsp7 and nsp8 cofactors. On the other hand the presence of only nsp7 or nsp8 antagonises the nsp12 activity[124]. While the short nsp7, with 83 amino acid residues, consists only of 4 α-helices, which are required for the nsp7-nsp8 complex assembly, nsp8 is a relatively longer protein, composed of 198 amino acids and possesses 2 domains. The highly flexible N terminal domain has positive charge and is likely involved in viral RNA binding. The C- terminal domain is conserved among *Coronaviruses* and helps the nsp7-nsp8 complex dimerization and tetramerization[115,125]. Nsp8 is also involved in the regulation of MHC expression and in the evasion of immune system recognition via disruption of MAVS complex assembly, STING signalling and attenuation of IFN response[126,127].

Nsp9 is a 113 amino acids-long ssDNA and ssRNA-binding dimeric protein involved in RTC formation and RNA replication. It potentially stabilizes replication intermediates, despite the RNA binding mechanism remaining unclear[115]. Furthermore, nsp9 weakens the NFκB-regulated gene expression, suppresses RIG-I expression hampering the immune response[128].

Nsp10 functions as a stabilising and stimulating cofactor for nsp14 and nsp16, enhancing their activities in proofreading and coronaviral RNA capping, respectively[115]. The positively charged nsp10's surface interacts with nsp16 hydrophobic pocket and stabilises thus the S-adenosylmethionine binding site. Particularly, nsp10 acts as methyltransferase (nsp16) stimulator to execute S-adenosylmethionine-dependent methyltransferase activity to

methylate ribose on 2'-O, hence being crucial for immune escape of the viral RNA[129]. Nsp10 139 amino acid long monomer folds in 12 identical subunits creating a hollow spherical dodecameric architecture[129].

Nsp11 is a short intrinsically disordered peptide resulting from the cleavage of the ORF1a polyprotein. Its exact function remains largely uncharacterised, but it is conserved among *Coronaviruses*. Some studies suggest that the 13 amino acids long nsp11 may have a structural or regulatory role in viral replication, aggregates formation or polyprotein processing, yet there is no definitive evidence or well-defined enzymatic activity attributed to it[130,131].

The RNA-dependent RNA polymerase (RdRp) nsp12 forms the RdRp holoenzyme together with one copy of nsp7 and two copies of nsp8[124]. Nsp12 is translated upon a ribosomal frameshift site at ORF1a/1b. A programmed −1 frameshifting event promoting the translation of ORF1b give rise to a nsp12-containing pp1ab polyprotein. The 932 amino acid residues long coding sequence contains 3 domains - RdRp-associated nucleotidyl-transferase domain, the interface domain, and the RdRp domain[115]. Nsp12 is the target of the FDA-approved antiviral drug remdesivir[132].

The nsp13 is a 601 aa-long helicase that unwinds dsRNA with a 5'-3' polarity during replication and hydrolyses 5′ triphosphate ends, an event crucial for genome stability and capping. Besides dsDNA and dsRNA helicase activity, nsp13 is also capable to unwind RNA-DNA duplex. The activity of nsp13 helicase is increased 2 times by the interaction with the RdRp nsp12[115,129].

Nsp14 is 527 aa protein with a with 2 functional domains both with enzymatic activity : a 3′→5′ exonuclease N-terminal domain that proofs newly synthesized RNA (increasing replication fidelity), and a C-terminal guanine-N7-methyltransferase domain involved in mRNA capping[44,115,133].

The nsp15 protein is composed of 346 amino acid residues and acts as an endoribonuclease. Nsp15 degrades viral RNA to prevent recognition by host sensors and promote immune escape. This nuclease is responsible for 3' cleavage of uridines in a manganese (Mn^{2+}) dependent manner and the cleavage of the 5' terminus polyuridine tract of the viral RNA negative strand[129,134].

Nsp16 is 298 amino acids long protein functioning as a catalytic part of 2′-O-methyltransferase. It is active only when supported by the nsp10 function as mentioned previously[115]. Nsp10-nsp16 interaction results in production of a cap structure on viral mRNAs that mimics host mRNAs, thereby making nsp16 an important player in evading innate immune detection. Interestingly, its deletion impairs replication only on a mild level[129,135].

Protein	Amino Acid length	Molecular weight (kDa)	Function
NSP1	180	19.8	Host translational shutdown
NSP2	638	70.5	Unclear; endosome-associated
NSP3	1945	217.3	Multiple; DMVs and membrane pore formation, PLpro protease
NSP4	500	56.2	DMVs and membrane pore formation; ER membrane curvature
NSP5	306	33.8	3CL protease
NSP6	290	33.0	DMVs connectors formation
NSP7	83	9.2	RTC core cofactor
NSP8	198	21.9	RTC core cofactor
NSP9	113	12.4	RTC formation
NSP10	139	14.8	Nsp14 and nsp16 stimulating and stabilising factor
NSP11	13	1.3	unknown
NSP12	932	106.7	RdRp, RTC catalytic core
NSP13	601	66.9	helicase
NSP14	527	59.8	Exonuclease, viral mRNA capping
NSP15	346	38.8	endoribonuclease
NSP16	298	33.3	2'-O-methyltransferase, viral mRNA capping

Table 1: Overview of SARS-CoV-2 non-structural proteins and their functions.

1.1.6.3.2 Accessory proteins

Besides the structural and non-structural proteins, SARS-CoV-2 encodes several accessory proteins that, while dispensable for viral replication, are important for host interaction and immune evasion, contributing to pathogenicity and virulence. The specific functions of individual ORFs remain largely elusive. Among the better characterised accessory proteins, ORF8 and ORF10 were connected to regulation of immune signalling, such as modulation of MHC-I expression or blocking of interferon type I signalling[90,136–138]. On the other hand, ORF3a and ORF7a were reported as important players in autophagy regulation and lysosomes deacidification for virus egress promotion. Both of these proteins are involved in block of autophagic flux through autophagosomes-lysosome fusion impairment[64,73,139–141].

The 275 amino acid ORF3a is the most abundant accessory protein of SARS-CoV-2 and is located between the S and E genes. It composes of three transmembrane domains, an N-terminal region, and a C-terminal region and is suggested to form a homo-oligomer[142,143]. Originally, ORF3a was proposed to be an ion-channel, although recently this function was disproven and rather replaced with the hypothesis of ORF3a being a lysosomal water-permeable channel, allowing deactivation of lysosomes through their deacidification and displacement of Rab7 from the TBC1D5-GAP-Rab7 complex[142,144]. Furthermore, ORF3a is indispensable for the block of autophagosome-lysosome fusion through its binding to Vps39 and blocking of the SNARE complex assembly and subsequent interaction with the HOPS complex components[73].

ORF7a codes for a 121 amino acid residues long protein and it possesses a single transmembrane domain, a N-terminal signalling region, an Ig-like ectodomain and an ER retention motif. It is involved in type-I interferon signalling, similarly to other virulence factors, and autophagy modulation[123,140,145]. ORF7a activates autophagosomes accumulation via AKT-MTOR-ULK1-regulation and simultaneously supports ORF3a-mediated block of fusion event by degrading SNAP29 protein through caspase cleavage[140].

1.2 Autophagy

Macroautophagy (hereafter only autophagy) is a crucial catabolic process which ensures the intracellular homeostasis, protection from pathogens and degradation of various cargo. The engulfment of cargo such as cellular debris, damaged organelles (mitophagy, ER-phagy), protein aggregates (aggrephagy), and pathogens (xenophagy) is dependent on the *de novo* formation of double-membraned vesicles called autophagosomes. Since autophagosomes are rapidly formed in cells, their growth is dependent on pre-existing donor membranes enriched in lipids and equipped with the enzymatic machinery that allows *de novo* lipid synthesis. The primary donor membrane site for nascent autophagosomes is the ER. In addition to lipid donor membranes, autophagosomes formation also involves lipid receiving membranes, known as membrane seed vesicles, which are capable of accepting lipids from the donor membranes. For example, Golgi derived ATG9 vesicles have been reported as membrane seed[146–148].

Autophagy is highly conserved among eucaryotes and most of its mechanistic processes were initially described in the yeast model. The characterization of autophagy-related genes (ATGs) in the yeast, laid the foundation for understanding the functions of their corresponding mammalian orthologues. The majority of the ATG proteins assemble into multi-subunit complexes that together coordinate the intricate process of autophagosome biogenesis. In humans, these complexes are the Unc-51-like autophagy activating kinase 1 (ULK1) complex, the autophagy-specific class III phosphoinositol-3-kinase (PI3K) complex, ATG9A-positive vesicles, the ATG2/WIPI4 complex, the ubiquitin-like (Ub-like) conjugation system proteins of ATG12 complex, the Ub-like conjugation system proteins of the ATG8 orthologues. The mammalian orthologues of the yeast ATG8 protein are represented by the microtubule-associated protein 1 (MAP1) light-chain 3 (LC3) and GABA type A receptor-associated protein (GABARAP) subfamily. In humans, a total of 6 paralogs belonging to both families – LC3A, LC3B, LC3C, GABARAP, GABARAPL1, GABARAPL2 (GATE16) are present. Although phylogenetical analysis showed that the GABARAP subfamily is evolutionarily closer to the yeast ATG8, the LC3 family proteins and N-terminus of yeast ATG8 share conformational similarities[149].

1.2.1 Autophagy regulation

Autophagy has a complex regulation mediated by post-translation modifications, mainly including phosphorylation and ubiquitination. In basal condition, autophagy is regulated by nutrients availability through the AMP and mTOR kinases, which act as a positive and negative regulator respectively, and phosphorylate ULK1 and PIK3 complexes. Autophagy activation is dependent on several factors, among which the presence of PI3P - a lipid species produced by PI3K and crucial for early autophagy. The PIK3 is activated through ULK1-mediated phosphorylation and inactivated by the mammalian target of rapamycin (mTOR) complex 1 mTORC1-dependent phosphorylation. mTOR is the main negative regulator of autophagy and senses the presence of nutrients within the cell. Amino acid starvation causes mTOR inactivation leading to partial dephosphorylation of ATG13, which in turn initiates the cascade of assemblies of autophagy activator complexes. ATG13 commence the activation of a ULK1 protein kinase complex formed by ULK1, ATG13, FAK family kinase-interacting protein of 200 kDa (FIP200, also called RB1CC1) and ATG101[150].

The ULK1 complex is subsequently recruited to the PI3P and ZFYVE1 rich omegasome, followed by the PI3K complex consisting of PI3K class 3 (PI3KC3, also called VPS34), phosphoinositide-3-kinase regulatory subunit 4 (PIK3R4), ATG14 and Beclin 1. As mentioned, phagophores can either derive directly from the ER membrane, or from other membrane sources, such as recycling endosomes, mitochondria, the Golgi apparatus or other membrane organelles. These so-called membrane seed vesicle subsequently establish membrane contact sites (MCS) with the ER to support phagophore membrane elongation[148,151].

1.2.2 Autophagosomes formation

Double membrane autophagosomes are briskly formed with a lifetime of approximately 20 minutes. They can vary in size from few hundred nanometres (nm) to more than 1 micrometre (μm), based on the size of the sequestered cargo. An average autophagosome vesicle of ~400nm can require recruitment of more than 3 000 000 lipids for its formation[150].

1.2.2.1 Omegasome and phagophore nucleation

The biogenesis of autophagosomes starts at the phagophore assembly site (PAS), also called omegasome, which has dual a function – serving as a phagophore scaffold, and

supplying the essential lipids. Omegasomes are specific ER subdomains which can be recognised by phosphoinositol-3-phosphate (PI3P) accumulation in response to autophagy initiation. Notably, in cells we distinguish two independent and unconnected PI3P pools, based on their co-localisation with either the double FYVE domain-containing protein 1 (ZFYVE1/DFCP1) marking omegasomes, or with WIPI proteins marking phagophores[152,153]. Omegasomes form either directly at the ER membranes e or at MCS between other organelles and the ER. Apart from classical bulk autophagy, omegasome formation has been described during mitophagy induced by the iron chelator deferiprone, by oligomycin/antimycin A treatment, or in Parkin-mediated mitophagy[151,154,155]. Omegasomes are characterised by their omega-shaped structure and play an indispensable role in autophagosome formation. They serve as platforms for phagophore (also called the initiation membrane) assembly and elongation from lipid-rich donor membranes, enabling the rapid formation of single of even multiple autophagosomes at the same time[151]. The accumulation of PI3P produced by phosphoinositide-3-kinase (PI3K) leads to recruitment of ZFYVE1 which allows the connection of the seed vesicle with the omegasome site driving the nascent phagophore formation. Nascent phagophore can be recognised in the cells by LC3B, p62, syntaxin 17 or WIPI2 staining, while ZFYVE1 is used as a main marker of omegasome[151,153,156]. Interestingly, ZFYVE1 mutants cause defects only in selective autophagy, while the bulk autophagy seems unaffected.

1.2.2.2 Phagophore expansion

The nucleated double-membrane sheet of the phagophore successively elongates from its rim via lipid transfer, mediated by the ATG12 and ATG8 conjugation systems. Supply of lipids required for the phagophore expansion is ensured mainly by the function of VMP1, ATG2 and ATG9 proteins[157–164]. VMP1 is a lipid scramblase at the omegasome site of ER, ATG2 locates at phagophore - ER MCS and in addition to establishing this connection, it transports the lipids into the outer membrane of the growing phagophore[148,165]. Finally, ATG9, which is the only transmembrane ATG protein, works as a lipid scramblase on phagophore site distributing lipids in the phagophore's inner membrane[159,160]. ATG2 is fundamental for establishing ER-phagophore MCS and its deletion leads to impairment of phagophore elongation and thus block in the autophagic flux[151]. Interestingly, reconstitution of only the small chorein domain of ATG2 is sufficient to tether membranes, even though the lack of the

channel activity leads to much less efficient lipid transfer activity[157,158,166]. ATG2 localisation and function on the phagophore site is controlled by the β-propeller domains that bind the polyphosphoinositides protein family, WIPI1, WIPI2, WIPI3 and WIPI4[167,168]. The dual function of ATG2 highlights the importance of this protein in phagophore growth. In addition to the ER-originating phosphatidylcholine (PC) and PI3P, the lipid supply in the elongating phagophore is probably also ensured by the lipid droplets (LDs) found in proximity to the crescent phagophore and associated with ATG2A and ATG9A. However, both the lipid transfer ,whether via LDs or through ER-mediated lipid transfer, and the exact lipid composition of the omegasomes remain elusive[169,170]. On the other hand, at least a portion of the phagophore is created by active phospholipid synthesis and direct integration of those lipids into the elongating phagophore [171]. The ER scramblase VMP1 also interacts with the ER-localized transmembrane protein TMEM41B, which is responsible for lipid mobilisation[162,163]. This further suggest that the ER-phagophore MCS are hotspots for bulk lipid production[162,172,173]. The lipid composition of growing phagophore is thought to affect the membrane curvature, as the lipids such as phosphatidylethanolamine (PE) and phosphatidic acid induce membrane curvature, while other lipids, such as PI, PC, and phosphatidylserine (PS), promote bilayer formation[150,174]. Interestingly, a theoretical modelling study of autophagosome formation suggested that, rather than requiring a specific machinery dedicated to curve the membrane, spherical autophagosomes arise through the release of membrane curvature energy from the *de novo* formed, flattened double-membrane phagophore sheet[175]. The conjugation of PE to autophagosomal membranes via LC3s and GABARAPs is mediated by two Ub-like conjugation systems. The conjugation of ATG8 family proteins to lipids is highly curvature-sensitive, with high curvature membranes promoting more efficient conjugation. Therefore the ATG8 family proteins are thought to localise preferentially at the highly curved edges of phagophores[176]. Apart from the localisation at highly curved regions that favour efficient LC3 lipidation, the presence of WIPI2 on the phagophore is also crucial, as its absence impairs phagophore's maturation into a functional autophagosome[151].

1.2.2.2.1 Ubiquitin-like conjugation systems

Two Ub-like systems are involved in autophagosomes formation: the ATG8 system, composed of Atg7 (an E1 enzyme), Atg3 (an E2 enzyme) and the ATG12 system, composed

of covalently bound ATG5, ATG12 and ATG16L1 (acting like an E3 enzyme). Both of these systems participate in the formation of an amide bond between the C-terminal carboxyl group of LC3/GABARAPs and the amino group in the hydrophilic head of the PE[177]. The conventional ATG8 conjugation process is well studied for the LC3 family proteins. The cytoplasmic proLC3 is initially cleaved by the ATG4 protease to uncover the C-terminal glycine, generating LC3-I[177]. LC3-I can be subsequently recognised by ATG7, which activates the glycine in an ATP-dependent manner, and then transfers it to ATG3 to form a thioester-bonded ATG3-LC3 intermediate[178]. The ATG12 system promotes allosteric changes in the ATG3 active site, that in turn mediates the binding of LC3-I to PE, thus forming LC3-II[178]. Interestingly, immunoblot analysis of LC3 reveals two distinct bands: the lipidated form (LC3-II) at approximately 18 kDa, and the non-lipidated form (LC3-I), which migrates as an apparently smaller band of around 16 kDa.

1.2.2.2.1.1 ATG8 homologues

There are 6 homologues of ATG8-family proteins in human, all derived from separate transcripts distributed from multiple genes on various chromosomes (Table 3). Nevertheless, their sequence is highly similar. LC3B is the best-characterized member of the ATG8 family and serves as a hallmark marker of autophagosomes. Other ATG8 homologues, LC3A, LC3C, GABARAP, GABARAPL1, and GABARAPL2, share approximately 92%, 71%, 59%, 60%, and 65% sequence identity with LC3B, respectively[179]. They belong to a broader group of small ubiquitin-like modifiers, that are structurally similari to ubiquitin, independent of the amino acid sequence. In addition, ATG8 proteins possess two distinctive N-terminal α-helices, that differ among the ATG8 homologues. While the first α helix of the LC3 subfamily is strongly basic, it is mostly acidic in the GABARAP proteins. The N-terminus of both LC3 and GABARAP proteins is involved in membrane tethering and fusion activity[180]. Similarly to ubiquitin, ATG8 proteins possess hydrophobic pockets enabling the docking with multiple ATGs via the LC3 interacting region (LIR). All ATG8 paralogues recognise the four core amino acid residues of the LIR in their interactors, regardless of whether they belong to the LC3 or GABARAP family. On the other hand, the substrate affinity and selectivity, however, are likely influenced by an extended LIR region encompassing up to 20 residues surrounding the core motif[181]. Homologues further differ in their expression levels across different tissues. For example, LC3A and LC3B are abundantly expressed in the heart, brain, skeletal muscle, and testis. On the other hand, LC3C is mainly expressed in lungs, placenta and ovaries, while its

expression in other tissues is generally lower than LC3A and LC3B levels[182]. These differences suggest that ATG8 homologues perform non-redundant functions. This is further supported by interactome analysis showing that in addition to a conserved core set of interactors, both LC3B and LC3C establish specific protein-protein interactions. LC3C was shown to interact with several factors involved in the omegasome and phagophore formation steps, such as ATG13, FIP200 and ATG9. Interestingly, LC3C puncta colocalise with ATG9-positive vesicles and endosomes in the cellular periphery and are temporarily recruited to crescent phagophores, while mainly perinuclear puncta of LC3B are observed in later steps of autophagosome formation. This difference in spatiotemporal distribution, likely mediated via the distinct extended C-terminal tail of LC3C, suggests that LC3C might be involved in the early steps of autophagy in manner distinct from LC3B[183] (Table 3).

name	C-terminus (C-terminal glycine highlighted)	length	location
LC3A	MVYASQETFGF	121	20q11.22
LC3B	MVYASQETFGMKLSV	125	16q24.2
LC3C	MTYASQETFGCLESAAPRDGSSLEDRPCNPL	147	1q43
GABARAP	IAYSDESVYGL	117	17p13.1
GABARAPL1	VAYSDESVYGK	117	12p13.31
GABARAPL2	VAYSGENTFGF	117	16q22.1

Table 2: ATG8 homologues in Homo sapiens.

The strict spatiotemporal regulation of ATG8 homologues recycling is controlled by post-translational modifications on the ATG4 proteases, such as phosphorylation, ubiquitination, O-GlcNacylation, S-nitrosylation and oxidation[184–189]. However, even direct modifications on LC3 and GABARAP subfamilies were reported. Specifically, Herhaus *et al*. described TBK1-mediated phosphorylation of LC3C and GABARAPL2, which disabled the ATG4 protease to recognise these substrates and therefore impaired their delipidation[190].

In general, ATG8 homologous proteins have indispensable role in autophagosome growth, selective cargo engulfment and lysosomal fusion. Mammalian homologues of ATG8 are, similarly to yeast ATG8, required for the expansion step, even though a delayed formation of

partially elongated membranes or even autophagosome-like structures can be found[149]. In the cells depleted of the components of ATG8 conjugation machinery autophagosomes can still be found, even though they are smaller in size, form at lower rate and are unable to fuse with lysosomes[191–193]. Even single LC3/GABARAP subfamily depletion can lead to autophagosome's size reduction, similarly to the complete knockout of all human ATG8 orthologues[193,194].

In addition to their role in membrane elongation, the spatiotemporal regulation and recycling of ATG8 homologues by ATG4 proteases also contribute to efficient lysosomal fusion[150]. Nevertheless, the functional diversity and non-canonical roles of individual homologues remain insufficiently characterized, and overlooking these aspects may lead to an incomplete understanding of ATG8 protein functions, underscoring the need for further investigation.

1.2.2.2.1.2 ATG4 proteases

ATG4 proteases are essential endopeptidases that play critical roles in the regulation of autophagy, a fundamental cellular degradation and recycling process. As mentioned, they mediate the proteolytic priming of ATG8 family proteins, by cleaving their C-terminal regions to expose a glycine residue essential for lipidation and attachment to the autophagosomal membrane. ATG4 proteases further regulate autophagy by removing lipidated ATG8 from autophagosomal membranes, maintaining the dynamic balance of ATG8 conjugation and deconjugation necessary for autophagosome biogenesis and maturation[195]. However, recent studies reveal that ATG4 proteases also promote autophagosome formation and phagophore expansion independently of their protease activity and ATG8 lipidation process, implicating additional non-canonical roles such as facilitating ATG9A vesicle trafficking and promoting phagophore-ER MCS essential for lipid transfer during autophagosome biogenesis[196,197].

The ATG4 protein family in mammals consists of four homologues - ATG4A, ATG4B, ATG4C and ATG4D. All homologues possess the C54 cysteine protease domain and LC3 interacting regions (LIR). For long time, ATG4s were thought to be redundant in their function. Lately, crucial insights into their differences were described by Kauffmann *et al.*, who described the preferences of the different ATG4s to soluble and membrane-bound ATG8 homologues[198]. They confirmed *in vitro* and in cells, that ATG4B is constitutively catalytically active, has a broad substrate specificity, and thus can be considered the main priming enzyme in LC3/GABARAP processing, likely due to its unique N-terminal LIR[198,199]. However, they also

demonstrated using a 4xATG4 KO system, that the sole reconstitution of ATG4B in the tetra KO cells fails to rescue the defect in delipidation, as the ATG4B deconjugation activity is intrinsically inefficient[198]. On the opposite end, ATG4D exhibits only weak priming activity, but functions predominantly as the main delipidating enzyme that removes lipidated ATG8 proteins from autophagosomal membranes, a critical step that regulates autophagosome maturation, lysosomal fusion and ATG8-proteins recycling [198,200]. ATG4A and ATG4C exhibit functional redundancy, yet nuances in substrate specificity compared to other ATG4s were observed[199]. ATG4A is active in priming only of soluble GABARAP subfamily proteins and shows 3-10 times slower priming activity than ATG4B. On the other hand, its deconjugation activity is faster than ATG4B, particularly on GABARAPL2 delipidation[198]. ATG4C shows only very weak priming activity, similarly to ATG4D. However, both of these proteins are much more efficient in PE-deconjugation, probably thanks to their C-terminal LIR, which was shown to be involved in the delipidation[196,198,200,201]. On the structural level, both ATG4C and ATG4D have extended N-terminal autoinhibitory domains containing canonical caspase cleavage sites (DEVDK motifs)[202–204]. For ATG4D, cleavage at this DEVDK motif has been proposed to modulate its enzymatic activity, potentially responsible for the weak GABARAPL1 priming capacity[203]. However, the triple ATG4A/B/C KO cells present lipidated GABARAPL1 and GABARAPL2 even upon Caspase3 KD, suggesting that even the full length ATG4D can possess priming activity[205–207]. Full-length ATG4C and ATG4D were also reported as the main delipidating enzymes in non-canonical ATG8 lipidation pathways, such as LC3- associated phagosomes (LAP) pathway, pharmacologically induced or viral infection activated conjugation of ATG8 to single membranes (CASM). In the latter, alternative lipidation with PS occurs and ATG4C-D variants were much more efficient in delipidating the PS-conjugated ATG8s[207]. ATG4D isoform 2 associates with mitochondria, thanks to an unmasked mitochondrial targeting motif, whereas in the full-length isoform 1 the cryptic mitochondrial targeting motif is revealed only upon caspase cleavage. The mitochondrial recruitment of both isoforms, together with the unique affinity of ATG4D for mitochondrial cardiolipin, support an unique role for this protein in the modulation of mitochondria-associated regulatory processes[203,208,209]. Indeed, ATG4D also harbours a putative Bcl-2 homology 3 (BH3) domain in its C-terminus potentially linking it to apoptosis regulation and highlighting its multifaceted role in cellular homeostasis[203,204].

The activity of ATG4 proteases is finely tuned by various post-translational modifications, including phosphorylation, S-nitrosylation, ubiquitination and H_2O_2 mediated oxidation as described on ATG4B and ATG4A examples[184,186,187,189,203]. The PTMs probably enable adaptation of autophagic flux in response to cellular stress. Further autoinhibitory conformations, regulatory N-termini and interfacial regulation of substrate binding highlight sophisticated regulatory mechanisms ensuring precise autophagy control[198]. Such intricate regulation, together with the coexistence of specific and overlapping functions of ATG4 proteases underscores their importance in efficient modulation of autophagy across diverse physiological and pathological conditions.

1.2.2.3 Phagophore closure and maturation of autophagosome

The phagophore extrusion is accompanied by the progressive omegasome constriction mediated by ZFYVE1 ATPase activity until omegasome's complete disappearance[155]. Finally, phagophore growth reaches the closure point and culminates into closed autophagosome vesicle. It is interesting to note that the whole lifetime of omegasomes takes only around 6 minutes and mature autophagosome is completed within 10 minutes, underlying how rapid is autophagosome biogenesis[151]. The very last scission step of a highly constricted phagophore membrane neck is mediated by the endosomal sorting complexes required for transport (ESCRT) machinery. The ESCRT-I components (VPS37A and VPS28) on the phagophore facilitate temporary recruitment of ESCRT-III components, including chromatin-modifying protein/charged multivesicular body protein 2A (CHMP2A) and the filament-forming subunit CHMP4B, bringing the two membranes of the phagophore edge in close proximity to allow membrane fusion[210–214]. The closed autophagosome is recognised by presence of STXN17 and removal of part of other ATG components, such as partial ATG4-mediated depletion of ATG8 homologues from the outer autophagosomal membranes, or PI3P removal by myotubularin family PI3P phosphatases Jumpy (MTMR14) and MTMR3[190,215]. Cargo-containing autophagosome (amphisome) decorated with LC3 then usually fuses with lysosomes within 10-20 minutes and forms autophagolysosome, where the low pH caused by hydrolases brought by lysosomes initiates the process of cargo degradation. The fusion of autophagosomes with lysosomes is mediated by small GTPases, the soluble *N*-ethylmaleimide-sensitive factor attachment protein receptors (SNAREs) complex and homotypic fusion and protein sorting (HOPS) tethering complex[216].

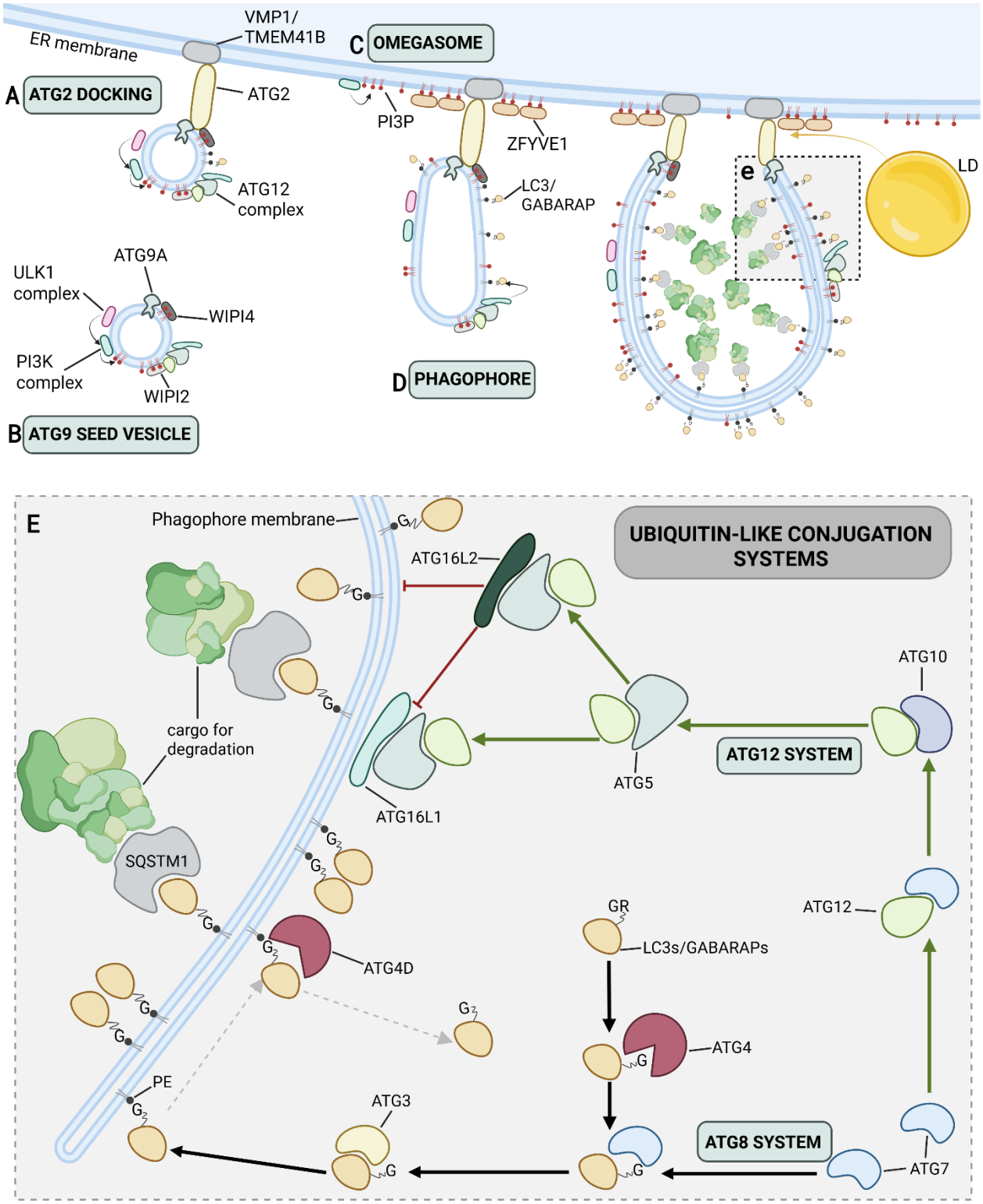

Figure 3: Scheme of autophagosome formation. **A** Recipient membrane for the autophagosome biogenesis is so called seed vesicle, which is for example of Golgi-originating ATG9A-vesicle. This probably bring components of the autophagy machinery, including PI3K and ULK1 complexes, and some core components required for LC3/GABARAP lipidation machinery. **B** Seed vesicles establish contact with the endoplasmic reticulum (ER) thanks to tethering protein ATG2, which binds to the transmembrane scramblases VMP1/TMEM41B in the ER membranes and as main component of establishes the phagophore-omegasome

membrane contact site. **C** Omegasome is the specific subdomain of the ER where initiates the actual phagophore formation. Omegasome is marked by presence of ZFYVE1 protein and accumulation of phosphatidylinositol 3-phosphate (PI3P) by action of PI3K complex type III. **D** Nascent phagophore starts to expand its membranes and engulf cargo thanks to function of lipid transferring machinery of ATG2-ATG9 and WIPI4 proteins and conjugation of LC3s/GABARAPs proteins to the phosphatidylethanolamine (PE). Lipid supply for very rapid membrane formation is ensured by the ER and probably also lipid droplets (LD). **e/E** The detail of Ubiquitin-like conjugation systems participating in phagophore elongation. Both of conjugation systems necessary for LC3s/GABARAPs proteins lipidation start at the E1-like enzyme ATG7. In ATG8 conjugation system, LC3 and GABARAPs proteins get primed to lipidation by the ATG4 proteases mediated cleavage, which expose their penultimate glycine residue enabling thus activation by ATG7. E2-like enzyme ATG3 subsequently transports LC3/GABARAPs to PE on phagophore membrane. This event probably occurs most efficiently at the rim of phagophore with a high membrane curvature. The ATG12 system also starts at ATG7 which activates the ATG12 protein. Subsequent E2-like enzymatic reaction with ATG10 enzyme allows ATG12 conjugation to a specific lysine residue on ATG5. The ATG5-ATG12 conjugate then forms an E3-like enzymatic complex with ATG16. The active form of this complex is created with ATG16L1 and facilitates conjugation of LC3s/GABARAPs proteins. The competitive ATG16L2 binding to ATG5-ATG12 conjugates results in inactive complex, unable to bind to autophagosomal membrane acting thus as lipidation inhibitor. Later occurring recycling of LC3 homologues is ensured by the main delipidating enzyme ATG4D.

1.2.3 Autophagy interplay with viruses

Autophagy is not only a fundamental pathway for cellular homeostasis, but also an important player in viral infections, although its impact varies among different families of viruses. Activation of degradative autophagy generally tends to impair viral infections, as the complete autophagic flux can help the infected cell to fight the pathogen through virus degradation (example of xenophagy) as well as use the autophagy for presentation of viral antigens and subsequent activation of immune responses.

On the other hand, a myriad of viruses can benefit from the initiation of non-degradative autophagy, particularly from the autophagic membranes formation[217–219]. Viruses with +ssRNA genome, such as Coronaviruses and Flaviviruses, replicate in the cytoplasm and their replication is strictly connected to creation of membranous replication organelles, therefore incorporating the machinery involved in induction of autophagosomes biogenesis can be favourable to infection outcomes[71].

1.2.3.1 Coronaviruses and autophagy

There are several reports on autophagy induction, autophagosome accumulation and or block of autophagosome fusion with lysosome in cells infected with Coronaviruses ranging from α- to δ-coronaviruses[122,220–222]. The α-coronavirus Porcine epidemic diarrhoea virus (PEDV)'s nsp6 and ORF3 proteins were shown to promote autophagy activation benefiting virus replication[222,223]. Similarly, nsp6 protein of several β- and γ- coronaviruses, including SARS-CoV and infectious bronchitis virus (IBV), recruits ZFYVE1 to omegasomes, leading to phagophore membranes nucleation and subsequent autophagosomes formation[122]. Another example of how are the autophagic factors repurposed for the virus's benefit was made by Reggiori *et al.*, who showed that the LC3-I (unlipidated form) is usurped by the mouse hepatitis virus (MHV) to promote virus replication[221]. They described an unconventional role of LC3s in the lipid-free form, that is independent on autophagy, where the non-lipidated LC3B coats viral-induced DMVs.

The importance of autophagy activation specifically in SARS-CoV-2 is demonstrated by the interaction of several viral protein with multiple autophagy regulation complexes, such as the role of PI3K in vROs formation[71]. Expression of several SARS-CoV-2's proteins, such as E, M, S, ORF3a and ORF7a, activates autophagy and subsequently leads to autophagosomes accumulation in transfected and infected cells through mTORC1 signalling impairment[71,75,224,225](Fig.4). The ULK1-mediated autophagy activation is induced by SARS-CoV-2 ORF7a and depletion of ORF7a is essential for efficient production of the viral progeny[140]. S protein induces autophagy similarly to ORF7a by inhibiting PI3K/AKT/mTOR signalling via reactive oxygen species upregulation in the cell[226] (Fig. 4). ORF3a causes augmentation of transcription factor EB (TFEB) nuclear localisation, which interestingly leads to the sole upregulation of genes for cathepsin D and cathepsin A, while most of the other TFEB-regulated genes remain unaffected[75,227]. In contrast to autophagy activation, SARS-CoV-2 subsequently blocks the autophagic flux through the activity of ORF7a and ORF3a (Fig. 4). The interaction of ORF3a with the HOPS complex member VPS39 impairs the STX17-SNAP29-VAMP8 SNARE complex assembly and blocks autophagosome-lysosome fusion resulting in accumulation of autophagosomes[73,139](Fig.4). Moreover, this effect is supported by ORF7a-mediated SNAP29 decrease in caspase 3-dependent manner[140]. The impaired autophagic flux and cargo degradation causes ER stress and potentially supporting

the formation of vROs by nsp proteins through ER membranes hijacking. The crucial role of the autophagosome-lysosome fusion is further highlighted by virus replication and propagation decrease upon pharmacological activation of autophagy, or ORF3a and ORF7a depletion[140,225]. The degradation of ER-membranes by ER-phagy is prevented also by the recruitment of ER-phagy receptors FAM134B and ATL3 to liquid droplet condensates formed by ORF8 and SQSTM1 (p62)[91]. Taken together, conventional degradative autophagy is dispensable, and potentially detrimental, for SARS-CoV-2. Interestingly, phagophore forming machinery responsible for autophagosomes creation seems to be required[228,229]. This further suggests that the autophagic machinery responsible for phagophore formation may be co-opted by SARS-CoV-2 to drive DMV biogenesis. ATG3, ATG16L1 and UVRAG upregulation upon SARS-CoV-2 infection was speculated to promote virus replication as virus particles were observed close to phagophore membranes in EM[229]. Phagophore-ER MCS establishment and particularly function of autophagy scramblases VMP1 and TMEM41B is required for vROs formation. While TMEM41B facilitates the NSP3-NSP4 interaction, VMP1-mediated PS distribution in nascent membranes was postulated to help the closure of the viral DMVs[72].

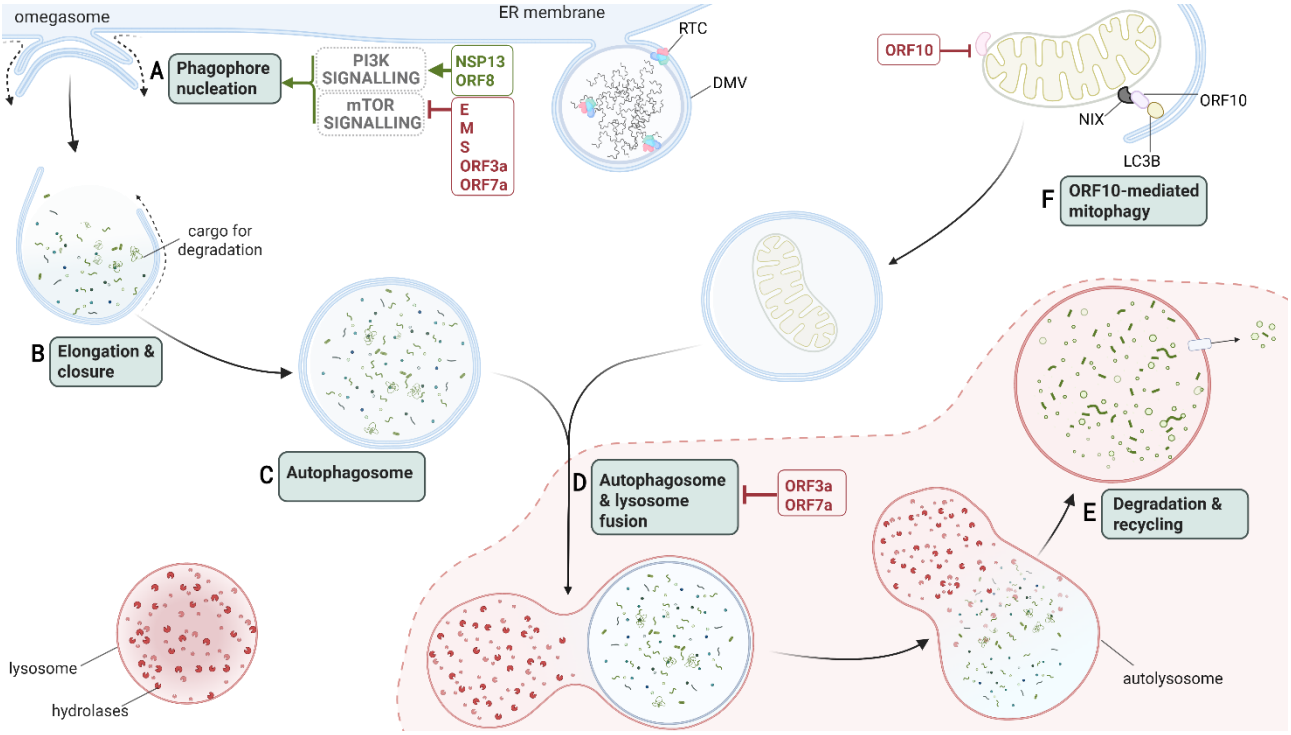

Figure 4: Scheme of reported SARS-CoV-2 effects on autophagy. SARS-CoV-2 infection activates autophagy by mTOR and PI3K signalling modulation via several of its structural (E, M, S), non-structural (NSP13) and accessory proteins (ORF3a, ORF7a, ORF8) and leads to subsequent autophagosomes accumulation in the

infected cell (**A–C**). The degradative part of the autophagy pathway is impaired thanks to the accessory proteins ORF3a and ORF7a blocking the autophagosome-lysosome fusion and thus all the following steps. (**D–E**). **F** ORF10 induces selective degradation of mitochondria (mitophagy) to suppress MAVS signalling and innate immune activation.

As previously mentioned, autophagy primary role lays in maintaining the cellular homeostasis, therefore the multifaceted nature of this pathway is implicated not only in pathogen degradation, but it also mediates the presentation of virus components to the host immune system. For this reason, SARS-CoV-2 evolved multiple ways for evasion of the antiviral innate immune response through rewiring selective autophagy processes. Counteraction of the innate immunity is mainly achieved by inhibition of the mitochondrial antiviral proteins signalling (MAVS) and subsequent interferon (IFN) type I and IFN stimulated genes (ISG) production[136,137]. The accessory protein ORF10 accomplishes this goal in a dual mode, first through mitophagy induction via the interaction with the mitophagy receptor Nip3-like protein X (NIX), leading to the recruitment of LC3B on the mitochondrial membranes and consequent MAVS degradation (Fig.4). Second, ORF10 inhibits the CGAS-STING1-IFN regulatory factor 3 (IRF3)-TANK binding kinase 1 (TBK1) activation and its interaction with STING[136]. Furthermore, NSP13 induces TBK1 degradation via selective autophagy in a p62-dependent manner[230]. Accessory protein ORF8 counteracts the immune response by targeting the major histocompatibility complex class I (MHC-I) into lysosomes via autophagy, which in turn diminishes antigen presentation and hinders the recognition of infected cells by T cells[90]. Lastly, modulation of autophagy was also reported in COVID-19 patients, where dysregulation of autophagy in peripheral lymphocytes lead to their apoptosis resulting in lymphopenia[231].

Even after the extensive research on the SARS-CoV-2 life cycle that occurred in recent years, many aspects of the host factors involved in the formation of viral replication organelles remain elusive. Consequently, our understanding of how this virus exploits autophagy-related factors also remains limited. Therefore, further investigation into the molecular interplay between SARS-CoV-2 and the autophagy machinery is required.

2 The aim of the thesis

This thesis aims to elucidate the host cell mechanisms underlying the formation and functional coordination of SARS-CoV-2 replication organelles, with a particular focus on autophagy-related proteins and in the appendix, proteins involved in the ER membrane dynamics.

Specifically, it investigates how autophagy factors—such as ATG4D and LC3C—and ER-shaping proteins, notably atlastin-2 (ATL2), contribute to the biogenesis, structural integrity, and spatial organisation of double-membrane vesicles (DMVs) and production of new virions. By integrating high-content siRNA screening, molecular reconstitution, and ultrastructural analysis, the work seeks to define the roles of these host factors in viral replication, virion assembly, and immune evasion, thereby providing a deeper understanding of host–virus interplay, with implications for the development of targeted antiviral strategies against SARS-CoV-2 and related coronaviruses.

3 Materials and Methods

3.1 Cell culture

A549 (ATCC; ATCC-CCL-185), Calu-3 (ATCC; ATCC-CRM-CCL-2), HeLa (ATCC; ATCC-CRM-CCL-2), HEK-293T (ATCC; ATCC-CRL-1573), MRC5 (ATCC, ATCC-CCL-171), and Vero E6 (ATCC, ATCC-CRL-1586) cells were cultured in Dulbecco's modified Eagle's medium (DMEM, Gibco) enriched with 10% fetal bovine serum (FBS, Euroclone), 2mM L-glutamine (Sigma-Aldrich), 1mM minimal Non-Essential Amino Acids, 1mM Sodium Pyruvate (Gibco), and 10 µg/mL Penicillin/Streptomycin (Gibco). HK2 cells were cultured in DMEM/ Nutrient Mixture F-12 (Gibco) supplemented with 5% FBS, 1% insulin-transferrin-selenium, 2mM L-glutamine and 10 µg/mL Penicillin/Streptomycin. HeLa ATG4 A/B/C triple KO cells, and ATG4 A/B/C/D tetra KO (ABM) were cultured in 10% fetal bovine serum (FBS, Euroclone), 25mM HEPES (Sigma-Aldrich), 2mM L-glutamine (Sigma-Aldrich), 1mM minimal Non-Essential Amino Acids, 1mM Sodium Pyruvate (Gibco), and 10 µg/mL Penicillin/Streptomycin (Gibco). All cell lines were maintained at 37 °C in a humidified incubator with 5% CO2 atmosphere. All the infections were performed in corresponding medium supplemented with 2% FBS instead of the 10% FBS. All cell lines are regularly tested for mycoplasma contamination.

3.2 Viruses

The SARS-CoV-2 isolate BavPat1/2020 p2, provided by Prof. Christian Drosten through the European Virology Archive (Ref-SKU: 026 V-03883) was propagated on Vero E6-TMPRSS2 cells infected with MOI 0.001 for 72 hours at 37° C. Collected supernatant was cleared of cell debris by centrifugation, filtered through 0.45 um filter and supplemented with 10mM HEPES. Viral titer was determined by plaque assay on Vero E6 cells. HCoV-OC43 (ATCC, VR-1558) virus was propagated on MRC5 cells infected with MOI 0.01 for 72 hours at 37° C. Collected supernatant was cleared of cell debris by centrifugation, filtered through 0.45 um filter, and supplemented with 10mM HEPES. Viral stock was determined by TCID50 assay on MRC5 cells. Viruses were stored at -80° C. All SARS-CoV-2 infections were performed in the BSL-3 laboratory of the Telethon Institute of Genetic and Medicine (TIGEM). Decontamination of infected samples was performed according to the biosafety manual of the BSL-3 laboratory.

All lentiviruses were produced by triple transfection of HEK-293T cells with gag-pol, VSVg and pWPI lentiviral plasmids constructs. Supernatant was collected after 72 hours, cell debris removed by centrifugation and filtering through 0.45 um filter, supplemented with 10mM HEPES and tittered through HeLa Kyoto based colonies assay. Lentiviruses were stored at -80°C.

3.3 Lentivirus production and titration

Lentiviral stocks were produced in 70% confluent HEK 293T cells transfected with packaging plasmids pCMV-Gag-Pol and pMD2-VSV-G and backbone plasmids encoding for different genes of interest (pWPI-ACE2, pWPI-ACE2-TMPRSS2, pWPI-EF1A-empty and pWPI-EF1A-ATL2B). 6 hours post-transfection the complete medium was replaced to 2% DMEM medium and 48hpt the medium containing the lentiviruses was collected cell debris removed by centrifugation and filtering through 0.45 um filter, supplemented with 10mM HEPES. Lentivirus aliquots were stored at -80°C.

Lentiviruses titration was performed in HeLa Kyoto strain, transduced with two dilutions of lentivirus preparation in presence of 4 µg/ml polybrene and then cultured for 5 days in presence of 1 µg/ml puromycin or 2 µg/ml blasticidin. The fifth day cells were washed and stained with 1% crystal violet/10% ethanol for 20 minutes. Stained cells were rinsed with water and number of colonies was used to calculate lentiviral titres.

3.4 Viral infections

Infections with SARS-CoV-2 were all performed in BSL-3 laboratory following the biosafety protocols. HCoV-OC43 and SARS-CoV-2 viral inoculum was prepared in culturing medium with reduced FBS (2%). Medium was removed from cells and viral inoculum was added on permissive cells in volumes adapted to plate format as mentioned in Table 4. Cells were incubated in humidified incubator with 5% CO_2 at 37°C. Viral inoculum was kept on cells for 2 hours in case of SARS-CoV-2 or 3 hours in case of HCoV-OC43 before removing it. Cells were washed 3 times with PBS and fresh 2% medium was added for the remaining time of infection.

Format	Volume [µl]
96-well plate	25
24-well plate	200

12-well plate	400
6-well plate	800
10 cm dish	4000

Table 3: Volumes of viral inoculum used for infection.

3.4.1 Atlastin 2 and 3 KO and OE cell lines

For infection experiments one million cells per 10 cm plate format of A549-ATL2/3 KO cells and A549-ATL2/3-HA overexpressing cells was transduced with lentivirus (viz Chapter 3.7), cells were incubated for 72h, detached and plated either in 24-well format with 60.000 cell/well or 6-well format with 300.000 cells/well. After 24 h, cells acutely expressing ACE2 and ATL2B, or ACE2-TMPRSS2 were infected with BAVPAT1 isolate of SARS-CoV-2 at MOI=5, or MOI=0.01 respectively. Viral inoculum was removed 2hpi, cells washed three times with PBS and further incubated with 2%FBS complete medium with the exception of the experiments needed for extracellular lysate WB, in which case cells were incubated with complete medium without FBS. Virus-containing supernatants were collected at 6, 10, 12, 16, 24, 48 and 72 hours for titres calculation by PFU assay. Cells were then washed twice with PBS, homogenised with homogenisation buffer supplemented with thioglycerol and lysed in lysis buffer from Maxwell® RSC simply RNA Cells Kit (Promega) for RNA extraction. Alternatively, cells for immunofluorescence were washed once with PBS and fixed with 4% EM grade PFA. To establish extracellular viral proteins, supernatant from infected cultured in no FBS complete medium cells in 6-well format were collected, centrifuged 5 minutes at 300g to remove cell debris and then concentrated to final volume of 90 ul using Amicon 10K Ultra Centrifuge columns and lysed in 6xSB. To collect intracellular lysates cells were washed once with PBS and lysed with RIPA buffer with PIP (Roche). Extracellular virus titers were determined by PFU assay. Extracellular infectivity and virus replication was analysed using quantification of viral RNA levels in supernatant or cells lysates respectively were assessed by RT-qPCR.

3.5 Plaque assay

SARS-CoV-2 titer was assessed by plaque assay. Vero E6 cells were seeded in 24-well plate at a density of 2.5 x 10^5 cells/well. After 24 hours the cell monolayer was inoculated with 10-fold dilutions of virus supernatants in technical duplicates and incubated at 37°C for 2

hours. Subsequently, the inoculum was aspired and 1ml of 0.9% carboxymethyl-cellulose (Sigma-Aldrich) in MEM (Gibco) was added to each well. Cells were incubated for 70 hours in humidified incubator at 37°C and 5% CO2 atmosphere. At 72 hours post infection cells were fixed in 5% formaldehyde for 30 minutes and the plate was transferred for another 30 minutes in 6% formaldehyde in PBS for complete virus inactivation to exit BSL-3 Laboratory. Inactivated plate was washed 3 times with tap water, wells were overlayed with 1% Crystal Violet (Sigma-Aldrich) for 15 minutes, then rinsed with tap water and plaque forming units (PFU)/ml were counted using average number of plaques in well from the technical duplicate, and dilution in which the plaques were counted.

3.6 $TCID_{50}$ assay

Quantification of viral titres in case of HCoV-OC43 was performed using $TCID_{50}$ assay. MRC5 cells were seeded in technical quadruplicates in 96-well plate with a density of 2.0 x 10^4 cells/well. The day after, the cell monolayer was inoculated with 10-fold dilutions of virus-containing supernatant and incubated for 96 hours. 96 hpi the supernatant was removed, and cells were fixed with 4% paraformaldehyde in PBS for 30 minutes. Fixed cells were washed once with PBS, permeabilised with 0.1% Triton X-100 in PBS for 10 minutes and washed with PBS again before adding a rabbit primary antibody against OC43 Nucleoprotein (Sino Biological, Cat #40643-T62). Plates were incubated with primary antibody at 37°C for 2 hours and then an anti-Rabbit secondary antibody AlexaFluor-488 conjugated was added for another 1-hour and incubated at 37°C in the dark. Secondary antibody was removed, washed with PBS and fluorescent wells were quantified using epifluorescent microscope to count FFU/ml and $TCID_{50}$/well.

3.7 Transduction

All transductions were performed in 10% FBS complete medium enriched with 4 ug/mL polybrene. Briefly, trypsinised cells were resuspended in 10% FBS complete medium and counted. 1.0 x 10^6 cells were resuspended in 10mL 10 %FBS complete medium supplemented with 4 ug/mL polybrene and further specified amount of lentivirus was added to the suspension. Cells were then plated in 10 cm diameter cell culture dish and incubated at 37°C in humidified incubator with 5% CO_2. For experiments requiring ACE2, or ACE2 and TMPRSS2 expression cells were transduced using 250 ul of specific lentivirus for each 1.0 x 10^6 cells. ATG4D isoform 1, as well as empty control were transduced with moi=10, ATG4D

isoform 2 with moi=1. Atlastin 2B and its mutants were transduced at moi=1 or moi=3 of lentivirus to achieve levels comparable to endogenous ones, or overexpression respectively. ATG7 KO guides were transduced using 500 uL lentivirus for 2.0 x 10^5 cells. Acute transductions were performed with 72 hours incubation with lentivirus and direct proceeding to seeding for particular experiment. In case of transductions for stable cell lines production, transduced cells were incubated with lentivirus for 24 hours, medium was then removed, and selection antibiotic was added and then changed every 48 hours, until all the cells in the killing control plate were dead. Concentration of antibiotics was determined for every separate cell line by generating a killing curve.

3.8 KO cell lines generation

Knockout of ATG4D and ATG7 in A549-ACE2 and Calu3 cell lines was generated following the protocol of Sanjana *et al*.[232]. The genome-scale CRISPR knock-out (GeCKO) libraries were used to select three different guideRNAs for each protein of interest and delivered into lentiCRISPRv2 one vector lentiviral system (GeCKO, Zhang Lab) containing two expression cassettes, hSpCas9 and the chimeric guide RNA. The vector was digested using BsmBI, and a pair of annealed oligos were cloned into the single guide RNA scaffold. Guides are listed in the Table 5. Two colonies per each guide were picked, plasmid extraction was performed using QIAGEN Plasmid Kits for Plasmid DNA Extraction. Plasmids sequences were confirmed through Sanger sequencing.

ATG7 sgRNA	sgRNA sequence (5'-3')
1a	AGAAGAAGCTGAACGAGTAT
1b	CTTGAAAGACTCGAGTGTGT
2a	TAGGGTCCATACATTCACTG

Table 4: Sequences of sgRNA for CRISPR/Cas9 mediated KO of ATG7.

3.9 Cell viability analysis

Cell viability was assessed using CellTiter-Glo® Luminescent kit (Promega) according to manufacturer's instructions. Briefly, 6,000 cells were plated in opaque-walled 96-well plates and incubated for at 37°C and 5% CO2. To measure cell viability at specific timepoints, cell culture medium was removed from each well and replaced with 100 µl of CellTiter-Glo® Reagent mixed with PBS (50% v/v). The plate was incubated at room temperature for 10

minutes to stabilize luminescent signal, which was then measured by the microplate reader (High-throughput screening microplate reader Synergy™ Neo BioTek Instruments).

3.10 Bacterial transformation and plasmid cDNA propagation

Plasmid DNA (1-20ng) was transformed in Stbl-3 bacteria (45 µl) using heat-shock method. Transformed bacteria were mixed with SOC medium (250 µl), agitated (300 rpm) for 1 hour at 37°C and then seeded on prewarmed Petri dish with selection antibiotic agar. Bacterial plates were incubated at 37°C ON. The following day, a single bacterial colony was inoculated into 5 ml of 2x Yeast Extract Tryptone medium (2xYT) containing 1 µg/ml ampicillin or 50 µg/ml kanamycin and incubated for 6 hours at 37 °C on a shaker (165 rpm). Next, the bacterial broth was diluted in 200 ml of 2xYT broth containing 1 µg/ml ampicillin or 50 µg/ml kanamycin and further incubated overnight at 37 °C on a shaker. The bacterial cells were harvested by centrifugation at 4500 x g for 15 minutes at 4 °C. Plasmid DNA was extracted from bacterial cultures with the Endo-free MaxiPrep kit (Qiagen) according to the manufacturer's instructions. Plasmid yield was determined by spectroscopy on Nanodrop 2000, UV-Vis Spectrophotometer (Thermo Scientific Inc).

3.11 Transfection

The HeLa cells were seeded in 24-well plate with coverslips in density of 4.0 x 10^4 cells/well in complete 10% FBS medium. The following day, the medium was replaced by fresh one. Transfection mix was prepared by diluting Lipofectamine 2000 transfection reagent (Thermofisher Scientific) in reduced serum OPTIMEM medium (Thermofisher Scientific), vortexing and incubating 5 minutes at RT before adding the plasmid DNA in OPTIMEM media prepared in separate reaction tube. The ratio of 3:1 was used, corresponding to 1.5 µL PEI and 0.5 µg DNA per well. After vortexing for 10 s, the mix was incubated 20 min at RT. Mixture was added to the cells drop by drop and then incubated for 30 hours-48hours.

3.11.1 Nsp3-nsp4 polyprotein expression

The transfection-based nsp3-nsp4 polyprotein expression system constructs previously described by Pahmeier *et al.* was used, as they conveniently allow following the nsps thanks to the affinity tags[233]. In our experiments we used eGFP and V5 affinity tags added to the N-terminus of nsp3 and C-terminus of nsp4. The transfection was performed using 1.2 ug DNA

per 24-well in 1:3 ratio with Lipofectamine 2000. Mixture was in case of polyprotein on cells for 16 hours.

3.12 Silencing using siRNA interference

Pools of three small-interfering RNAs targeting different autophagy factors together with the positive control ACE2 and a non-targeting control were acquired from Dharmacon. For further validation of ATG4D KD effect, two individual siRNA targeting ATG4D, ACE2 and non-targeting control siRNA were purchased from Ambion (Thermoscientific) and pooled together. 5x concentrated mastermix (100 nM) for silencing was prepared by adding siRNA pool to OPTIMEM (mixture A) and OPTIMEM containing the Lipofectamine RNAiMAX (ThermoFisher) transfection reagent (mixture B). Both mixtures were added together, homogenised by pipetting and incubated 30 min at RT. Then the 5x concentrated master mix was added to cells in 10% complete medium to achieve 1x concentration (20nM siRNA). Cells were incubated in humidified incubator with 5% CO_2 for 48 hours.

3.13 Immunofluorescence

Infected and mock A549 cells were grown on glass coverslips with density 50.000 cells/well in 24-well plate format. At specific times post-infection cells were fixed with 4% EM grade paraformaldehyde (PFA) in PBS at room temperature for 30 min. Then, whole plates were submerged in 4% PFA for another 30 minutes to be taken out of BSL-3 laboratory. PFA was removed and cells washed with PBS 2x. The permeabilization and blocking of cells was performed in saponin buffer (0.05% saponin, 0.5% BSA, and 50 mM NH4Cl in PBS) for 30 minutes. Coverslips were incubated with the primary antibodies at 4°C overnight or room temperature (RT) for 2 hours (Table 6). Coverslips were washed with PBS-0.01% Tween-20 and incubated with secondary antibodies for 1 hour at RT. Cells were then washed with PBS-0.01% Tween-20, stained for 15 minutes with Hoechst 33342, washed with ddH2O and mounted on the microscope slides using ProLong™ Glass Antifade Mountant™.

Antibody anti-	Origin	Dilution	Manufacturer	Identifier Cat.#
SARS-CoV-2 N	Mouse	1:1000	Sino Biological	40143-MM05
SARS-CoV-2 nsp3	Rabbit	1:1000	Genetex	GTX135589
HCoV-OC43 N	Rabbit	1:2000	Sino Biological	40643-T62
dsRNA	Mouse	1:500	Scicons	10010500

LC3B	Rabbit	1:500	MBL	PM036
HA	Rabbit	1:400	Sigma-Aldrich	H6908100UL
V5	Mouse	1:500	Sino Biological	100378-MM04
TOMM20	Mouse	1:400	BD	612278
ATL-2	Rabbit	1:200	Sigma-Aldrich	HPA075302
PDI	Rabbit	1:1000	Sigma-Aldrich	P7496
Alexa Fluor Plus 488 anti-mouse IgG (H+L)	Goat	1:800	Invitrogen	A32723
Alexa Fluor 488 anti-mouse IgG1	Goat	1:800	Invitrogen	A21121
Alexa Fluor 488 anti-mouse IgG2A	Goat	1:800	Invitrogen	A21131
Alexa Fluor 488 anti-mouse IgG2B	Goat	1:800	Invitrogen	A21134
Alexa Fluor 488 anti-rabbit	Goat	1:800	Invitrogen	A32731
Alexa Fluor Plus 568 anti-mouse IgG (H+L)	Goat	1:800	Invitrogen	A11031
Alexa Fluor 568 anti-mouse IgG1	Goat	1:800	Invitrogen	A21124
Alexa Fluor 568 anti-mouse IgG2A	Goat	1:800	Invitrogen	A21141
Alexa Fluor 568 anti-mouse IgG2B	Goat	1:800	Invitrogen	A21144
Alexa Fluor 568 anti-rabbit	Goat	1:800	Invitrogen	A11011
Alexa Fluor 647 anti-mouse	Goat	1:800	Invitrogen	A11011
Alexa Fluor 647 anti-rabbit	Goat	1:800	Invitrogen	A32733
Hoechst		1:10000		

Table 5: Primary and secondary antibodies used for immunofluorescent staining.

3.14 qRT-PCR

The total RNA was extracted using Maxwell® RSC simply RNA Cells Kit (Promega) according to the manufacturer's protocol. cDNA was synthesized from 200-400 ng of RNA with LunaScript RT SuperMix Kit according to manufacturer's instruction. A 1:20 dilution of the cDNA was used directly for qPCR analysis using specific primers (primer sequences in Table 7) and PowerUp SYBR Green Master Mix for qPCR (Applied Biosystems). The mRNA relative abundance from each sample was evaluated based on its cycle threshold (ct) values normalized to hypoxanthine phosphoribosyltransferase 1 (HPRT) transcript levels.

Primer name	Sequence 5'-3'
HPRT1_fw	CCTGGCGTCGTGATTAGTG
HPRT1_rev	ACACCCTTTCCAAATCCTCAG
TMPRSS2_fw	CCTCTAACTGGTGTGATGGCGT
TMPRSS2_rev	TGCCAGGACTTCCTCTGAGATG
ACE2_fw	TCA AGG AGG CCG AGA AGT TC
ACE2_rev	TTC CTG GGT CCG TTA GCA TG
SARS-CoV-2 Subgenomic RNA_fw	TCCCAGGTAACAAACCAACCAACT
SARS-CoV-2 Subgenomic RNA_rev	AAATGGTGAATTGCCCTCGT
HCoV-OC43 ORF1a_fw	TGCATCCCGTTTCACTGATC
HCoV-OC43 ORF1a_rev	AGAGGTAGCAGTTTGCTTGG
ATG4D_fw	CCAGCCCACTGTGGATGTC
ATG4D_rev	AAGCCCACGGTACAGCTTG
ATG7_fw	ATGATCCCTGTAACTTAGCCCA
ATG7_rev	CACGGAAGCAAACAACTTCAAC
ZFYVE1_fw	TGGTGCGGACAGAGATTGTG
ZFYVE1_rev	GACACCGACTGAGCCATGAA
PARK2_fw	GTGTTTGTCAGGTTCAACTCCA
PARK2_rev	GAAAATCACACGCAACTGGTC
ATG14_fw	TTCAGAGGCATAATCGCAAACT
ATG14_rev	CCAGACGCTCATAATGACTTCTT
ATG3_fw	GATGGCGGATGGGTAGATACA

ATG3_rev	TCTTCACATAGTGCTGAGCAATC
MAP1LC3C_fw	CCCAAGCGTCAGACCCTTC
MAP1LC3C_rev	GGGGAACTTTGCCCGGATT
GABARAPL2_fw	ACTCGCTGGAACACAGATGC
GABARAPL2_rev	TCTGAGAGCCTGAGACCTTTT
SQSTM1_fw	AAGCCGGGTGGGAATGTTG
SQSTM1_rev	CCTGAACAGTTATCCGACTCCAT
PIK3C3_fw	GTCTGGCCTAATGTAGAAGCAG
PIK3C3_rev	GGCAAGACGGCTCATCTGAT
ATL2_fw	ATGAGTTCTGCCGTCGTTATCA
ATL2_rev	TAGCAAACATGACCGCAAACA
ATL3_fw	GCCTTTCCAGACACTGATGTT
ATL3_rev	CCTTCACCTGTAAACGCTTATCC
MX1_fw	ACCATTCCAAGGAGGTGCAG
MX1_rev	TGCGATGTCCACTTCGGAAA
IFIT1_fw	GAAGCAGGCAATCACAGAAA
IFIT1_rev	TGAAACCGACCATAGTGGAA

Table 6: Primers used for q-RT-PCR.

3.15 Western Blot

Cells were washed with PBS and lysed in RIPA lysis buffer supplemented with protease inhibitor cocktail (Complete EDTA-free, Sigma-Aldrich), incubated 20 minutes on ice and centrifuged at 20000 g for 10 minutes in table-top centrifuge. Protein amount in the sample was quantified Bradford Protein Measurement Assay (BioRad). 20-25 ug of protein was mixed with 6x sample buffer (375 M Tris-HCl at pH 6.8, 12% SDS, 60% Glycerol, 0,6 M DTT, 0,6% bromophenol blue) to achieve 1x concentration and denaturated for 5 minutes at 95°C. Total protein was resolved by homemade SDS-PAGE, mPAGE™ 4-12% or 4-20% Bis-Tris Precast Gel (Sigma-Aldrich) MOPS running buffer (Thermofisher) and transferred to polyvinylidene fluoride (PVDF) 0.45 µm membrane (0.2 µm PVDF membrane for LC3B blotting) for 90 minutes at constant current – 250 mA for all proteins except of LC3B, which was transferred at 200 mA. Membranes were blocked with 3% BSA or 5% skimmed milk in TBS-T (TBS with 0.1% Tween-20) for 1 hour at room temperature. Incubation with primary

antibodies was performed overnight at 4°C. Used antibodies are listed in Table 8. Membranes were washed three times with TBS-T and incubated for 1 hour with horseradish peroxidase (HRP)-conjugated secondary antibodies in TBS-Tween (0.1%). Chemiluminescent signal was captured using the ECL system. Image processing and band analysis was performed using Fiji software (NIH).

Antibody anti-	Origin	Dilution	Manufacturer	Identifier Cat.#
GAPDH	Mouse	1:5000	Santa Cruz Biotechnology	sc365062
vinculin	Mouse	1:5000	Santa Cruz Biotechnology	sc-73614
β-actin	Mouse	1:5000	Sigma-Aldrich	A5441
LC3B	Mouse	1:1000	Nanotools	NTL0231100
HA	Mouse	1:1000	Biolegend	901501
HA for IP	Rat	1:1000	Roche	11867423001
ATG7	Rabbit	1:1000	Cell Signaling	8558
p62 (SQSTM1)	Mouse	1:1000	Cell Signaling	88588
N (SARS-CoV-2)	Rabbit	1:1000	Cell Signaling	26369
M (SARS-CoV-2)	Rabbit	1:1000	Prof. Machamer	Custom made
S½(SARS-CoV-2)	Mouse	1:1000	Cell Signaling	52342S
E (SARS-CoV-2)	Rabbit	1:1000	Prof. Machamer	Custom made
ACE2	Mouse	1:250	R&D Biotechne	MAB9332-100
ATL2	Rabbit	1:500	Sigma-Aldrich	HPA075302
ATL3	Rabbit	1:1000	Sigma-Aldrich	HPA065702
anti Rabbit IgG (whole molecule) peroxidase	Goat	1:6000	Sigma-Aldrich	A6154
anti Mouse IgG (whole molecule) peroxidase	Goat	1:6000	Sigma-Aldrich	A4416
anti Rat IgG (whole molecule) peroxidase	Goat	1:6000	Thermo Scientific	31470

Table 7: Antibodies used for WB.

3.16 Immunoprecipitation for phosphosites detection mass spectrometry analysis

HeLa cells were seeded with density of 1.2x10^6 cells per dish in 10 cm dishes working in technical triplicates for each condition. The day after seeding, cell medium was replaced for 2% FBS DMEM medium. Cells were transfected with 12 ug of HA-tagged ATG4D isoform 1 or isoform 2 using Lipofectamine 2000 in ratio 1:3. 4 hours after transfection, medium was replaced with 4ml of fresh 2% FBS DMEM medium or with 4ml of moi=5 of HCoV-OC43 in 2%FBS DMEM and cells were incubated 3 hours at 37°C 5% CO2. Inoculum or mock medium was removed; cells washed two times with PBS and overlayed with 10 ml of fresh 2% FBS DMEM medium and incubated for 31 hpi at 37°C in humidified incubator with 5% CO_2. After 31 hours, the medium was removed, cells were washed 3 times with PBS and either 10% FBS DMEM or EBSS starvation medium with 100nM Bafilomycin A was added. Cells were incubated for 3 hours, then medium was removed and cells were washed once with PBS. Cells were scraped in 150µl of Total Lysis Buffer (1% SDS, 50 mM Tris pH 7.5, 1 mM EDTA, 25 mM NaF) supplemented with fresh protease inhibitors (cOmplete EDTA-free protease inhibitor cocktail, Sigma -Aldrich) to prevent protein degradation and phosphatase inhibitor cocktail 2 and phosphatase inhibitor cocktail 3 to prevent loss of phosphosites. Lysate was promptly transferred in 1350 µl of Normal Lysis Buffer (NL;150 mM NaCl, 50 mM Hepes, 1 mM EDTA, 1 mM EGTA, 10% (v/v) glycerol, 1% (v/v) Triton X-100, 10 µM $ZnCl_2$, 25 mM NaF) enriched of protease inhibitors and phosphatase inhibitors cocktails. All the following steps were performed strictly on ice. Lysates were incubated with 1ul of Benzonase for 20 minutes and samples were then centrifuged at 15,000 × *g* for 10 min at 4°C. The supernatant was transferred into a fresh tube. For input control 50 µl of sample was transferred to a new tube, mixed with 4xLDL NuPage buffer, denaturated at 95°C for 10 minutes and stored for WB. The rest of the sample was mixed with 20 µl of antiHA-agarose beads slurry (Sigma-Aldrich) and incubated overnight at 4°C with constant rotation. The following day, the mix was centrifuged for 90 seconds at 2000rpm. Supernatant was carefully removed using 27G ¾'' needle and three washes with 1ml of NL buffer were performed. All NL buffer was removed after the last wash and samples were washed with 500 µl of 1M UREA. Another 2 washes were performed with 500 µl of IP-wash buffer (50 mM HEPES pH 7.5, 150 mM NaCl, 200 mM Guanidiniumhydrochloride, 1mM edta, 25 mM NaF, 0,1 % Sodiumdeoxycholate). Beads were pelleted by centrifugation and 20 ul of Elution buffer (50 mM triethylammonium bicarbonate (TEAB), 2% Sodiumdesoxycholate (SDC), 5 mM Tris (2-carboxyethyl) phosphine (TCEP), 20

mM Chloroacetamide (CAA)) was added to the beads. After elution samples were digested in 0.5 ug LysC and incubated for 3 hours at 37°C and 850 rpm. Next, samples were diluted in 20 µl of 50mM TEAB and protein digestion continued with 0.5 ug of Trypsin at 37°C and 850rpm overnight. Peptides were desalted and concentrated using SDB-RPS StageTips and processed for LC-MS.

3.17 Pellet embedding

Cells grown in 6-well plate format were washed once with PBS and then fixed with 1% glutaraldehyde (GA) in 0.2 M HEPES (pH-7.3!) buffer 0.5 ml/12well for 30min at RT. Then washed once with PBS and wells were filled with 4% EM grade PFA for another 30 minutes to exit the BSL-3 laboratory. Afterwards, 3 washes with PBS were performed and cells were overlayed with 500 ml/well of 1% BSA diluted in PBS 1X. Cells were scraped and centrifuged at 13200rpm for 10 minutes, to obtain cell pellet. Post-fixation was performed by incubation with a mixture of 2% OsO4 and 3% potassium ferrocyanide on ice for 30 minutes. Pellet was washed three times with ddH2O, incubated for 5 minutes with 1% thiocarbohydrizide diluted in H2O, washed again and treated with 0.5% uranyl acetate overnight at 4°C. After the incubation pellets were rinsed with water, progressively dehydrated with increasing concentrations of ethanol (50% to 100%) and treated with 100% acetone. Then the mixture of acetone and epon was added and cells subsequently embedded in a polymerizing Epon for 48 h at 60°C. Embedded cells were cut in 70-nm thick sections by using a Leica UC7 microtome and a diamond knife (Diatome).

3.18 Bioinformatic analysis

Images were analysed with the Fiji image analysis software. Graphs and statistical analysis were performed using GraphPad Prism software. Schemes were created in BioRender. Image panels were designed in Adobe Illustrator. Statistical significance was assessed using a one-sample t-test against comparing experimental values with the theoretical mean of 1 of control cells (ns [not significant] $p > 0.05$, *$p < 0.05$, **$p < 0.01$, ***$p < 0.001$, **** $p < 0.0001$).

4 Results

4.1 LC3B accumulates upon SARS-CoV-2 infection

As previously reported[71,75,224,225], SARS-CoV-2 infection leads to the accumulation of LC3B associated to autophagosomes (Fig 4). Consistently, infection of A549-ACE2-TMPRSS2 for 24 to 72 hours with SARS-CoV-2 showed an increase signal of both LC3B and SQSTM1 by immunoblot (Panel 1a). Moreover, infected cells, positive for the viral N protein marker, showed an increase in LC3B puncta number per cell, commonly associated with autophagosomal-associated LC3-II, compared to uninfected cells, were LC3B signal was mainly cytoplasmic (dashed line in Panel 1b). Quantification of LC3B puncta in mock and infected cells at 24hpi and confirmed that in our model system autophagosomes SARS-CoV-2 infection induced LC3B accumulation.

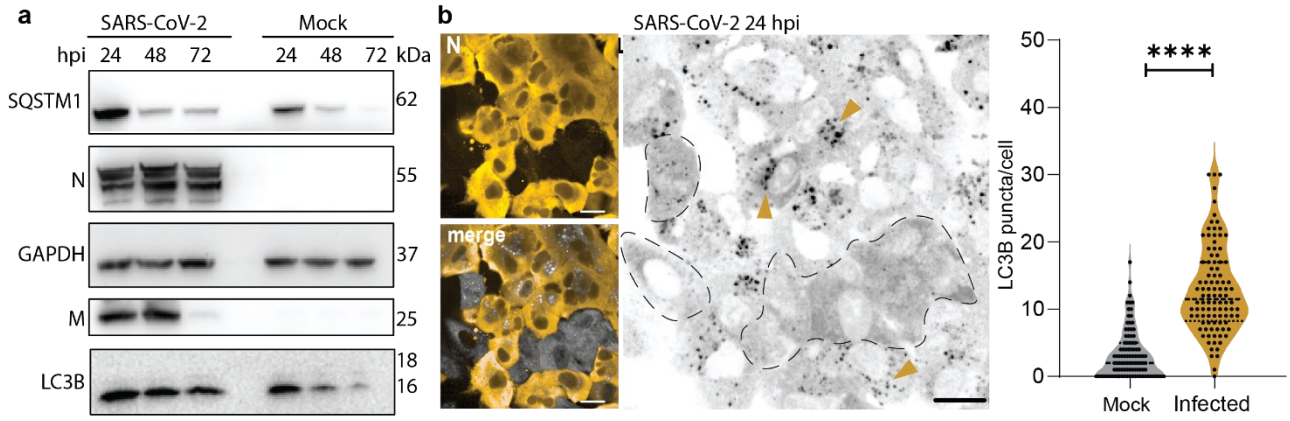

Panel 1: LC3B accumulates upon SARS-CoV-2 infection. a SDS-PAGE and immunoblot analysis of A549-ACE2-TMPRSS2 cells using antibodies to the SQSTM1, SARS-CoV-2 N and M proteins and LC3B. GAPDH was used as a loading control. Cells were collected at 24-, 48- and 72-hours post-infection prior to lysis. Uninfected cells served as control. **b** Representative image of LC3B puncta accumulation in infected 549-ACE2-TMPRSS2 cells. The cells were infected with SARS-CoV-2 for 24 hours, permeabilised and stained for N protein (yellow) and LC3B (grey). Scale bars: 20 µm. Yellow arrows indicate accumulation of LC3 puncta in infected cells. Dashed line indicates mock cells. Right panel, quantification of LC3B puncta in mock and infected cells. Each dot represents one cell (N=100). Statistical significance was determined using t-test (ns [not significant], $p > 0.05$, *$p < 0.05$, **$p < 0.01$, ***$p < 0.001$, ***$p < 0.0001$).

4.2 siRNA screening revealed multiple novel dependency and restriction factors affecting replication and or assembly of SARS-CoV-2.

The role of the autophagy pathway in SARS-CoV-2 viral cycle has been extensively studied; still, it is still unclear why viral infection both activates the autophagy pathway and subsequently blocks it at the step of autophagosome – lysosome fusion. While the degradative activity of autophagy can limit viral infection, SARS-CoV-2 may rely on early autophagy components for replication and later inhibit autophagosome–lysosome fusion to evade clearance.

5 Appendix

5.1 Introduction to ER-shaping proteins

The endoplasmic reticulum (ER) is the largest organelle in eukaryotic cells with a fundamental role in a wide array of cellular processes, such as sterol, lipid and protein synthesis, protein modification and quality control, vesicular transport and Calcium ions (Ca^{2+}) signalling regulation[237]. The ER exhibits remarkable structural diversity, consisting of morphologically distinct subdomains ranging from ribosome-decorated membrane sheet-like cisternae (rough ER) and smooth ribosome-free vesicles (transient ER) in perinuclear area to tubule-like structures formed by smooth ER extending into the cytoplasm to reach the cell periphery, underpinning its functional versatility in protein synthesis, processing and interaction with other organelles[237,238]. The ER subdomains are not static; but rather the ER is a highly dynamic network where tubules are continuously formed, retracted, and remodelled. This dynamic nature allows the ER to adapt to the changing needs of the cell and to facilitate processes of lipid exchange, calcium signalling, and organelle biogenesis.

The unique morphology of the tubular network is maintained by two evolutionarily conserved protein families: the reticulons (RTNs) and Receptor Expression Enhancing Proteins (REEP/DP1/Yop1)[239]. These proteins contain hydrophobic hairpin elements that may include charged or proline residues, collectively referred to as reticulon homology domain (RHD). This domain is both necessary and sufficient for the generation of ER tubules. Insertion of the RHD into the outer leaflet of the ER membrane induces its curvature, thereby promoting tubule formation and maintaining their stability[239]. While RTNs and DP1/Yop1p are critical for tubule formation, the integration of these tubules into an interconnected network requires membrane fusion events. This is achieved at three-way junctions, which are small, triangular sheet areas with negatively curved edges. The 3-way junctions' formation, abundance and stability are mediated by another group of ER-shaping proteins – atlastins (ATLs) and Lunapark (LNPK)[240]. ATLs are ER-resident, membrane-bound GTPases belonging to the dynamin superfamily[241]. Through their GTPase activity, they mediate the homotypic fusion events required for tubules ends connection thus balancing their intrinsic instability[241,242]. On the other hand, Lunapark depletion accelerates ER tubule-to-sheet conversion, indicating that this class of proteins are dispensable for three-way junction formation but are required for their stabilization via ATL ubiquitination by its N-terminal ubiquitin ligase-like domain. [243–

[245]. Orso *et al.* provided and experimental evidence of the ATLs' fusion activity using Drosophila atlastin orthologue and proteoliposomes. They demonstrated that ATLs are required for ER tubule production in vitro and disruption of ATL function leads to the formation of long, unbranched ER tubules, highlighting their crucial role in fusion[242]. Interestingly, atlastins not only fuse membranes at three-way junctions, facilitating the connection of tubules into a continuous branched network, but also participate in the adjacent membrane-tethering function, mediate the lipid droplet size and modulate autophagy, supporting even broader role in ER organelle architecture[242,246].

Three ATL paralogues with differential expression are present in mammalian cells. Atlastin 1 (ATL1) can be found mainly in neural cells, while the other two members – atlastin 2 (ATL2) and atlastin 3 (ATL3) are expressed more ubiquitously[240]. ATLs possess two closely spaced transmembrane domains after short cytoplasmic C-tail, three-helix bundle and GTPase domain on the N-terminus connected by a linker region[247]. The C-terminus likely acts in membrane tethering, while the homotypic fusion interactions are regulated by GTP binding and hydrolysis after ATLs undergo nucleotide-dependent homodimerization[248,249]. ATLs localise to the ER tubules thanks to the ER retrieval motif and subsequently interact with RTN and DP1 family proteins through their transmembrane domains on the C-terminal side, on the other hand, the N-terminal domain is cytoplasmic and is dispensable for that interaction[240]. The transmembrane domains further contain potential cholesterol-binding motifs supporting atlastins role in the lipid droplet dynamics[250]. These three proteins were thought to be mostly redundant in their functions[250,251]. However, there is recent evidence pointing out for different involvement of ATL paralogues in ER-regulation, ER-phagy as well as in the response to Zika and Dengue virus infection, where ATL2 plays role in the replication of the virus, while ATL3 mainly affects virus assembly and release[252–255].

5.1.1 Atlastin 2

The evolutionary recent ATL2's C-terminal amphipathic α-helix acts as autoinhibitory domain and is suggested to play role in upregulation of ER-tubules fusion activity when the demand increases. Indeed, the full-length ATL2 protein almost completely lacks fusion activity and the C-terminal deletion leads to a 500-fold increase in membrane fusion accompanied by the 5-fold increase in membrane tethering [256,257]. ATL2 exists in five variants (ATL2-1/-2, … ,-5) generated by alternative splicing and the most common ATL2-1 isoform, considered the

canonical one, is only weakly active, due to the presence the inhibitory C-terminus. Interestingly, the common full-length ATL2-1 isoform contains 3 negatively charged amino acid residues in its C-terminal amphipathic helix and these residues seem to be essential for the activity of the autoinhibitory domain, as their replacement with non-polar amino acids leads up to 100-fold increase of fusion activity. On the other hand, the differentially expressed ATL2-2 splice variant has two out of the 3 negative residues in amphipathic α-helix replaced with positively charged arginine and these small differences lead to much higher fusion activity pointing out to differences in the role of splice variants based on their prevalent expression in different tissues. Taken together the fusion activity is tightly regulated by the charge in the residues of the adjacent helix. However, the tethering activity depends more on the whole autoinhibitory domain. Finally, the actual fusion and tethering activity are performed solely thanks to the GTP binding as the K107A nucleotide mutant in the GTPase domain leads to the complete loss of any fusion and tethering. While the fusion activity requires homodimers crossover conformation, the tethering is still maintained in the K372E crossover mutant[256].

5.1.2 Atlastin 3

Differently from the other two human homologues, ATL3 lacks the C-terminal autoinhibitory domain, and although its dimerization affinity is lower than that of ATL2, it is still able to restore fusion activity in ATL triple knockout cells. Therefore, it has been proposed to function as a constitutively active catalyst of membrane fusion[257]. Jang *et al*. furthermore suggested that the constitutively active ATL3 can support the role of the autoinhibited ATL2, as these two proteins can also form heterodimers[250,256]. Besides its canonical roles, ATL3 uniquely functions as an ER-phagy receptor capable of binding ATG8 homologues, in contrast to ATL2.[254]. ATL3 regulates ER-tubules turnover downstream of FAM134B in physiological conditions as well as in the context of infection[91,254].

5.2 Aims:

This project was a collaborative effort between Mirko Cortese's and Antonella De Matteis' laboratories at TIGEM, and Emory University (USA) and aimed on unravelling the potential involvement of ATLs in SARS-CoV-2 infection.

5.3 Note:

All the following experiments with nsp3-nsp4 protein transfection were performed by Simona Ricciardi. All the experiments with SARS-CoV-2 infection were performed by Štěpánka Vlachová.

Bibliography:

1. Menachery, V. D., Graham, R. L. & Baric, R. S. Jumping species—a mechanism for coronavirus persistence and survival. *Curr. Opin. Virol.* **23**, 1–7 (2017).

2. Woo, P. C. Y. *et al.* Discovery of Seven Novel Mammalian and Avian Coronaviruses in the Genus Deltacoronavirus Supports Bat Coronaviruses as the Gene Source of Alphacoronavirus and Betacoronavirus and Avian Coronaviruses as the Gene Source of Gammacoronavirus and Deltacoronavirus. *J. Virol.* **86**, 3995–4008 (2012).

3. Vijgen, L. *et al.* Complete Genomic Sequence of Human Coronavirus OC43: Molecular Clock Analysis Suggests a Relatively Recent Zoonotic Coronavirus Transmission Event. *J. Virol.* **79**, 1595–1604 (2005).

4. Ramos, J. L. *Microbial Biotechnology* 2022 and onwards. *Microb. Biotechnol.* **15**, 5–5 (2022).

5. Masters, P. S. The Molecular Biology of Coronaviruses. in *Advances in Virus Research* vol. 66 193–292 (Elsevier, 2006).

6. Cui, J., Li, F. & Shi, Z.-L. Origin and evolution of pathogenic coronaviruses. *Nat. Rev. Microbiol.* **17**, 181–192 (2019).

7. Zhou, P. *et al.* A pneumonia outbreak associated with a new coronavirus of probable bat origin. *Nature* **579**, 270–273 (2020).

8. Berry, D. M., Cruickshank, J. G., Chu, H. P. & Wells, R. J. H. The structure of infectious bronchitis virus. *Virology* **23**, 403–407 (1964).

9. Fehr, A. R. & Perlman, S. Coronaviruses: An Overview of Their Replication and Pathogenesis. in *Coronaviruses* (eds Maier, H. J., Bickerton, E. & Britton, P.) vol. 1282 1–23 (Springer New York, New York, NY, 2015).

10. Li, F. Structure, Function, and Evolution of Coronavirus Spike Proteins. *Annu. Rev. Virol.* **3**, 237–261 (2016).

11. Yogo, Y., Hirano, N., Hino, S., Shibuta, H. & Matumoto, M. Polyadenylate in the Virion RNA of Mouse Hepatitis Virus. *J. Biochem. (Tokyo)* **82**, 1103–1108 (1977).

12. Kim, D. *et al.* The Architecture of SARS-CoV-2 Transcriptome. *Cell* **181**, 914-921.e10 (2020).

13. McIntosh, K., Becker, W. B. & Chanock, R. M. Growth in suckling-mouse brain of 'IBV-like' viruses from patients with upper respiratory tract disease. *Proc. Natl. Acad. Sci.* **58**, 2268–2273 (1967).

14. Lau, S. K. P. *et al.* Molecular Epidemiology of Human Coronavirus OC43 Reveals Evolution of Different Genotypes over Time and Recent Emergence of a Novel Genotype due to Natural Recombination. *J. Virol.* **85**, 11325–11337 (2011).

15. Wang, C. *et al.* Antigenic structure of the human coronavirus OC43 spike reveals exposed and occluded neutralizing epitopes. *Nat. Commun.* **13**, 2921 (2022).

16. Zhang, Y. *et al.* Genotype shift in human coronavirus OC43 and emergence of a novel genotype by natural recombination. *J. Infect.* **70**, 641–650 (2015).

17. Hulswit, R. J. G. *et al.* Human coronaviruses OC43 and HKU1 bind to 9- *O* -acetylated sialic acids via a conserved receptor-binding site in spike protein domain A. *Proc. Natl. Acad. Sci.* **116**, 2681–2690 (2019).

18. Zhang, Z. *et al.* Two novel human coronavirus OC43 genotypes circulating in hospitalized children with pneumonia in China. *Emerg. Microbes Infect.* **11**, 168–171 (2022).

19. Oong, X. Y. *et al.* Identification and evolutionary dynamics of two novel human coronavirus OC43 genotypes associated with acute respiratory infections: phylogenetic, spatiotemporal and transmission network analyses. *Emerg. Microbes Infect.* **6**, 1–13 (2017).

20. Zhu, Y. *et al.* A novel human coronavirus OC43 genotype detected in mainland China. *Emerg. Microbes Infect.* **7**, 1–4 (2018).

21. Lau, S. K. P. *et al.* Fatal Pneumonia Associated With a Novel Genotype of Human Coronavirus OC43. *Front. Microbiol.* **12**, 795449 (2022).

22. Li, W. *et al.* Angiotensin-converting enzyme 2 is a functional receptor for the SARS coronavirus. *Nature* **426**, 450–454 (2003).

23. Hoffmann, M. *et al.* SARS-CoV-2 Cell Entry Depends on ACE2 and TMPRSS2 and Is Blocked by a Clinically Proven Protease Inhibitor. *Cell* **181**, 271-280.e8 (2020).

24. Li, W. *et al.* Bats Are Natural Reservoirs of SARS-Like Coronaviruses. *Science* **310**, 676–679 (2005).

25. Zhong, N. *et al.* Epidemiology and cause of severe acute respiratory syndrome (SARS) in Guangdong, People's Republic of China, in February, 2003. *The Lancet* **362**, 1353–1358 (2003).

26. Peiris, J. *et al.* Clinical progression and viral load in a community outbreak of coronavirus-associated SARS pneumonia: a prospective study. *The Lancet* **361**, 1767–1772 (2003).

27. Leung, G. M. *et al.* The Epidemiology of Severe Acute Respiratory Syndrome in the 2003 Hong Kong Epidemic: An Analysis of All 1755 Patients. *Ann. Intern. Med.* **141**, 662–673 (2004).

28. Zaki, A. M., Van Boheemen, S., Bestebroer, T. M., Osterhaus, A. D. M. E. & Fouchier, R. A. M. Isolation of a Novel Coronavirus from a Man with Pneumonia in Saudi Arabia. *N. Engl. J. Med.* **367**, 1814–1820 (2012).

29. Assiri, A. *et al.* Epidemiological, demographic, and clinical characteristics of 47 cases of Middle East respiratory syndrome coronavirus disease from Saudi Arabia: a descriptive study. *Lancet Infect. Dis.* **13**, 752–761 (2013).

30. Raj, V. S. *et al.* Dipeptidyl peptidase 4 is a functional receptor for the emerging human coronavirus-EMC. *Nature* **495**, 251–254 (2013).

31. Zumla, A., Hui, D. S. & Perlman, S. Middle East respiratory syndrome. *The Lancet* **386**, 995–1007 (2015).

32. Drosten, C. *et al.* Transmission of MERS-Coronavirus in Household Contacts. *N. Engl. J. Med.* **371**, 828–835 (2014).

33. Lu, R. *et al.* Genomic characterisation and epidemiology of 2019 novel coronavirus: implications for virus origins and receptor binding. *The Lancet* **395**, 565–574 (2020).

34. Kim, J.-M. *et al.* Identification of Coronavirus Isolated from a Patient in Korea with COVID-19. *Osong Public Health Res. Perspect.* **11**, 3–7 (2020).

35. Holmes, E. C. *et al.* The origins of SARS-CoV-2: A critical review. *Cell* **184**, 4848–4856 (2021).

36. Matsuyama, S. *et al.* Enhanced isolation of SARS-CoV-2 by TMPRSS2-expressing cells. *Proc. Natl. Acad. Sci.* **117**, 7001–7003 (2020).

37. Santín, C., Doerr, S. H., Pausas, J. G., Underwood, E. C. & Safford, H. D. No evidence of suitability of prophylactic fluids for wildfire prevention at landscape scales. *Proc. Natl. Acad. Sci.* **117**, 5103–5104 (2020).

38. Marano, V., Vlachová, Š., Tiano, S. M. L. & Cortese, M. A portrait of the infected cell: how SARS-CoV-2 infection reshapes cellular processes and pathways. *Npj Viruses* **2**, 66 (2024).

39. Kim, D. *et al.* The Architecture of SARS-CoV-2 Transcriptome. *Cell* **181**, 914-921.e10 (2020).

40. Bhatt, P. R. *et al.* Structural basis of ribosomal frameshifting during translation of the SARS-CoV-2 RNA genome. *Science* **372**, 1306–1313 (2021).

41. Gorbalenya, A. E., Snijder, E. J. & Ziebuhr, J. Virus-encoded proteinases and proteolytic processing in the Nidovirales. *J. Gen. Virol.* **81**, 853–879 (2000).

42. Malone, B., Urakova, N., Snijder, E. J. & Campbell, E. A. Structures and functions of coronavirus replication–transcription complexes and their relevance for SARS-CoV-2 drug design. *Nat. Rev. Mol. Cell Biol.* **23**, 21–39 (2022).

43. V'kovski, P., Kratzel, A., Steiner, S., Stalder, H. & Thiel, V. Coronavirus biology and replication: implications for SARS-CoV-2. *Nat. Rev. Microbiol.* **19**, 155–170 (2021).

44. Snijder, E. J., Decroly, E. & Ziebuhr, J. The Nonstructural Proteins Directing Coronavirus RNA Synthesis and Processing. in *Advances in Virus Research* vol. 96 59–126 (Elsevier, 2016).

45. Hillen, H. S. *et al.* Structure of replicating SARS-CoV-2 polymerase. *Nature* **584**, 154–156 (2020).

46. Angelini, M. M., Akhlaghpour, M., Neuman, B. W. & Buchmeier, M. J. Severe Acute Respiratory Syndrome Coronavirus Nonstructural Proteins 3, 4, and 6 Induce Double-Membrane Vesicles. *mBio* **4**, e00524-13 (2013).

47. Ricciardi, S. *et al.* The role of NSP6 in the biogenesis of the SARS-CoV-2 replication organelle. *Nature* **606**, 761–768 (2022).

48. Zimmermann, L. *et al.* SARS-CoV-2 nsp3 and nsp4 are minimal constituents of a pore spanning replication organelle. *Nat. Commun.* **14**, 7894 (2023).

49. Snijder, E. J. *et al.* A unifying structural and functional model of the coronavirus replication organelle: Tracking down RNA synthesis. *PLOS Biol.* **18**, e3000715 (2020).

50. Cortese, M. *et al.* Integrative Imaging Reveals SARS-CoV-2-Induced Reshaping of Subcellular Morphologies. *Cell Host Microbe* **28**, 853-866.e5 (2020).

51. Klein, S. *et al.* SARS-CoV-2 structure and replication characterized by in situ cryo-electron tomography. *Nat. Commun.* **11**, 5885 (2020).

52. Masters, P. S. The Molecular Biology of Coronaviruses. in *Advances in Virus Research* vol. 66 193–292 (Elsevier, 2006).

53. Sola, I., Almazán, F., Zúñiga, S. & Enjuanes, L. Continuous and Discontinuous RNA Synthesis in Coronaviruses. *Annu. Rev. Virol.* **2**, 265–288 (2015).

54. Wolff, G. *et al.* A molecular pore spans the double membrane of the coronavirus replication organelle. *Science* **369**, 1395–1398 (2020).

55. Chen, A. *et al.* A coronaviral pore-replicase complex links RNA synthesis and export from double-membrane vesicles. *Sci. Adv.* **10**, eadq9580 (2024).

56. Boersma, S. *et al.* Translation and Replication Dynamics of Single RNA Viruses. *Cell* **183**, 1930-1945.e23 (2020).

57. Xu, R., Shi, M., Li, J., Song, P. & Li, N. Construction of SARS-CoV-2 Virus-Like Particles by Mammalian Expression System. *Front. Bioeng. Biotechnol.* **8**, 862 (2020).

58. Plescia, C. B. *et al.* SARS-CoV-2 viral budding and entry can be modeled using BSL-2 level virus-like particles. *J. Biol. Chem.* **296**, 100103 (2021).

59. Katiyar, H., Arduini, A., Li, Y. & Liang, C. SARS-CoV-2 Assembly: Gaining Infectivity and Beyond. *Viruses* **16**, 1648 (2024).

60. McBride, C. E., Li, J. & Machamer, C. E. The Cytoplasmic Tail of the Severe Acute Respiratory Syndrome Coronavirus Spike Protein Contains a Novel Endoplasmic Reticulum Retrieval Signal That Binds COPI and Promotes Interaction with Membrane Protein. *J. Virol.* **81**, 2418–2428 (2007).

61. Monje-Galvan, V. & Voth, G. A. Molecular interactions of the M and E integral membrane proteins of SARS-CoV-2. *Faraday Discuss.* **232**, 49–67 (2021).

62. Jennings, B. C., Kornfeld, S. & Doray, B. A weak COPI binding motif in the cytoplasmic tail of SARS-CoV-2 spike glycoprotein is necessary for its cleavage, glycosylation, and localization. *FEBS Lett.* **595**, 1758–1767 (2021).

63. Ghosh, S. *et al.* β-Coronaviruses Use Lysosomes for Egress Instead of the Biosynthetic Secretory Pathway. *Cell* **183**, 1520-1535.e14 (2020).

64. Chen, D. *et al.* ORF3a of SARS-CoV-2 promotes lysosomal exocytosis-mediated viral egress. *Dev. Cell* **56**, 3250-3263.e5 (2021).

65. Mendonça, L. *et al.* Correlative multi-scale cryo-imaging unveils SARS-CoV-2 assembly and egress. *Nat. Commun.* **12**, 4629 (2021).

66. Scherer, K. M. *et al.* SARS-CoV-2 nucleocapsid protein adheres to replication organelles before viral assembly at the Golgi/ERGIC and lysosome-mediated egress. *Sci. Adv.* **8**, eabl4895 (2022).

67. Chen, D., Zhao, Y. G. & Zhang, H. Endomembrane remodeling in SARS-CoV-2 infection. *Cell Insight* **1**, 100031 (2022).

68. Li, M. *et al.* LLPS of FXR proteins drives replication organelle clustering for β-coronaviral proliferation. *J. Cell Biol.* **223**, e202309140 (2024).

69. Williams, J. M., Chen, Y.-J., Cho, W. J., Tai, A. W. & Tsai, B. Reticulons promote formation of ER-derived double-membrane vesicles that facilitate SARS-CoV-2 replication. *J. Cell Biol.* **222**, e202203060 (2023).

70. Nardacci, R. *et al.* Evidences for lipid involvement in SARS-CoV-2 cytopathogenesis. *Cell Death Dis.* **12**, 263 (2021).

71. Twu, W.-I. *et al.* Contribution of autophagy machinery factors to HCV and SARS-CoV-2 replication organelle formation. *Cell Rep.* **37**, 110049 (2021).

72. Ji, M. *et al.* VMP1 and TMEM41B are essential for DMV formation during β-coronavirus infection. *J. Cell Biol.* **221**, e202112081 (2022).

73. Miao, G. *et al.* ORF3a of the COVID-19 virus SARS-CoV-2 blocks HOPS complex-mediated assembly of the SNARE complex required for autolysosome formation. *Dev. Cell* **56**, 427-442.e5 (2021).

74. Huang, Y. *et al.* Molecular architecture of coronavirus double-membrane vesicle pore complex. *Nature* **633**, 224–231 (2024).

75. Koepke, L., Hirschenberger, M., Hayn, M., Kirchhoff, F. & Sparrer, K. M. Manipulation of autophagy by SARS-CoV-2 proteins. *Autophagy* **17**, 2659–2661 (2021).

76. Banerjee, A. K. *et al.* SARS-CoV-2 Disrupts Splicing, Translation, and Protein Trafficking to Suppress Host Defenses. *Cell* **183**, 1325-1339.e21 (2020).

77. Thoms, M. *et al.* Structural basis for translational shutdown and immune evasion by the Nsp1 protein of SARS-CoV-2. *Science* **369**, 1249–1255 (2020).

78. Xia, H. *et al.* Evasion of Type I Interferon by SARS-CoV-2. *Cell Rep.* **33**, 108234 (2020).

79. Yuan, S., Balaji, S., Lomakin, I. B. & Xiong, Y. Coronavirus Nsp1: Immune Response Suppression and Protein Expression Inhibition. *Front. Microbiol.* **12**, 752214 (2021).

80. Justo Arevalo, S. *et al.* What do we know about the function of SARS-CoV-2 proteins? *Front. Immunol.* **14**, 1249607 (2023).

81. Bouayad, A. Innate immune evasion by SARS-CoV-2: Comparison with SARS-CoV. *Rev. Med. Virol.* **30**, 1–9 (2020).

82. Cheng, N. *et al.* Protein post-translational modification in SARS-CoV-2 and host interaction. *Front. Immunol.* **13**, 1068449 (2023).

83. Isobe, A. *et al.* ACE2 N-glycosylation modulates interactions with SARS-CoV-2 spike protein in a site-specific manner. *Commun. Biol.* **5**, 1188 (2022).

84. Shajahan, A., Pepi, L. E., Kumar, B., Murray, N. B. & Azadi, P. Site specific N- and O-glycosylation mapping of the spike proteins of SARS-CoV-2 variants of concern. *Sci. Rep.* **13**, 10053 (2023).

85. Bouhaddou, M. *et al.* The Global Phosphorylation Landscape of SARS-CoV-2 Infection. *Cell* **182**, 685-712.e19 (2020).

86. Lu, S. *et al.* The SARS-CoV-2 nucleocapsid phosphoprotein forms mutually exclusive condensates with RNA and the membrane-associated M protein. *Nat. Commun.* **12**, 502 (2021).

87. Bouhaddou, M. *et al.* SARS-CoV-2 variants evolve convergent strategies to remodel the host response. *Cell* **186**, 4597-4614.e26 (2023).

88. Li, W. *et al.* Stability of SARS-CoV-2-Encoded Proteins and Their Antibody Levels Correlate with Interleukin 6 in COVID-19 Patients. *mSystems* **7**, e00058-22 (2022).

89. Gavilán, E., Medina-Guzman, R., Bahatyrevich-Kharitonik, B. & Ruano, D. Protein Quality Control Systems and ER Stress as Key Players in SARS-CoV-2-Induced Neurodegeneration. *Cells* **13**, 123 (2024).

90. Zhang, Y. *et al.* The ORF8 protein of SARS-CoV-2 mediates immune evasion through down-regulating MHC-I. *Proc. Natl. Acad. Sci.* **118**, e2024202118 (2021).

91. Tan, X. *et al.* Coronavirus subverts ER-phagy by hijacking FAM134B and ATL3 into p62 condensates to facilitate viral replication. *Cell Rep.* **42**, 112286 (2023).

92. Hoffmann, M. *et al.* SARS-CoV-2 Cell Entry Depends on ACE2 and TMPRSS2 and Is Blocked by a Clinically Proven Protease Inhibitor. *Cell* **181**, 271-280.e8 (2020).

93. Hoffmann, M., Kleine-Weber, H. & Pöhlmann, S. A Multibasic Cleavage Site in the Spike Protein of SARS-CoV-2 Is Essential for Infection of Human Lung Cells. *Mol. Cell* **78**, 779-784.e5 (2020).

94. Wang, S. *et al.* Sequential glycosylations at the multibasic cleavage site of SARS-CoV-2 spike protein regulate viral activity. *Nat. Commun.* **15**, 4162 (2024).

95. Xia, X. Domains and Functions of Spike Protein in SARS-Cov-2 in the Context of Vaccine Design. *Viruses* **13**, 109 (2021).

96. Nal, B. *et al.* Differential maturation and subcellular localization of severe acute respiratory syndrome coronavirus surface proteins S, M and E. *J. Gen. Virol.* **86**, 1423–1434 (2005).

97. Kuzmin, A., Orekhov, P., Astashkin, R., Gordeliy, V. & Gushchin, I. Structure and dynamics of the SARS-CoV -2 envelope protein monomer. *Proteins Struct. Funct. Bioinforma.* **90**, 1102–1114 (2022).

98. Zhou, S. *et al.* SARS-CoV-2 E protein: Pathogenesis and potential therapeutic development. *Biomed. Pharmacother.* **159**, 114242 (2023).

99. Nieto-Torres, J. L. *et al.* Severe Acute Respiratory Syndrome Coronavirus Envelope Protein Ion Channel Activity Promotes Virus Fitness and Pathogenesis. *PLoS Pathog.* **10**, e1004077 (2014).

100. Duart, G., García-Murria, M. J. & Mingarro, I. The SARS-CoV-2 envelope (E) protein has evolved towards membrane topology robustness. *Biochim. Biophys. Acta BBA - Biomembr.* **1863**, 183608 (2021).

101. Duart, G. *et al.* SARS-CoV-2 envelope protein topology in eukaryotic membranes. *Open Biol.* **10**, 200209 (2020).

102. Boson, B. *et al.* The SARS-CoV-2 envelope and membrane proteins modulate maturation and retention of the spike protein, allowing assembly of virus-like particles. *J. Biol. Chem.* **296**, 100111 (2021).

103. Siu, Y. L. *et al.* The M, E, and N Structural Proteins of the Severe Acute Respiratory Syndrome Coronavirus Are Required for Efficient Assembly, Trafficking, and Release of Virus-Like Particles. *J. Virol.* **82**, 11318–11330 (2008).

104. Zhang, Y. *et al.* Synthesis, insertion, and characterization of SARS-CoV-2 membrane protein within lipid bilayers. *Sci. Adv.* **10**, eadm7030 (2024).

105. Zhang, Z. *et al.* Structure of SARS-CoV-2 membrane protein essential for virus assembly. *Nat. Commun.* **13**, 4399 (2022).

106. Swann, H. *et al.* Minimal system for assembly of SARS-CoV-2 virus like particles. *Sci. Rep.* **10**, 21877 (2020).

107. Boson, B. *et al.* The SARS-CoV-2 envelope and membrane proteins modulate maturation and retention of the spike protein, allowing assembly of virus-like particles. *J. Biol. Chem.* **296**, 100111 (2021).

108. Marques-Pereira, C. *et al.* SARS-CoV-2 Membrane Protein: From Genomic Data to Structural New Insights. *Int. J. Mol. Sci.* **23**, 2986 (2022).

109. Cubuk, J. *et al.* The SARS-CoV-2 nucleocapsid protein is dynamic, disordered, and phase separates with RNA. *Nat. Commun.* **12**, 1936 (2021).

110. Bessa, L. M. *et al.* The intrinsically disordered SARS-CoV-2 nucleoprotein in dynamic complex with its viral partner nsp3a. *Sci. Adv.* **8**, eabm4034 (2022).

111. Bai, Z., Cao, Y., Liu, W. & Li, J. The SARS-CoV-2 Nucleocapsid Protein and Its Role in Viral Structure, Biological Functions, and a Potential Target for Drug or Vaccine Mitigation. *Viruses* **13**, 1115 (2021).

112. Thorne, L. G. *et al.* Evolution of enhanced innate immune evasion by SARS-CoV-2. *Nature* **602**, 487–495 (2022).

113. Thoms, M. *et al.* Structural basis for translational shutdown and immune evasion by the Nsp1 protein of SARS-CoV-2. *Science* **369**, 1249–1255 (2020).

114. Schubert, K. *et al.* SARS-CoV-2 Nsp1 binds the ribosomal mRNA channel to inhibit translation. *Nat. Struct. Mol. Biol.* **27**, 959–966 (2020).

115. Yan, W., Zheng, Y., Zeng, X., He, B. & Cheng, W. Structural biology of SARS-CoV-2: open the door for novel therapies. *Signal Transduct. Target. Ther.* **7**, 26 (2022).

116. Rut, W. *et al.* Activity profiling and crystal structures of inhibitor-bound SARS-CoV-2 papain-like protease: A framework for anti–COVID-19 drug design. *Sci. Adv.* **6**, eabd4596 (2020).

117. Alhammad, Y. M. O. *et al.* The SARS-CoV-2 Conserved Macrodomain Is a Mono-ADP-Ribosylhydrolase. *J. Virol.* **95**, e01969-20 (2021).

118. Qin, B. *et al.* Identification of the SARS-unique domain of SARS-CoV-2 as an antiviral target. *Nat. Commun.* **14**, 3999 (2023).

119. Kifer, A. *et al.* Orchestration of SARS-CoV-2 Nsp4 and host cell ESCRT proteins induces morphological changes of the endoplasmic reticulum. *Mol. Biol. Cell* **36**, ar40 (2025).

120. Wang, P., Tian, B., Xiao, K., Ji, W. & Li, Z. The SARS-CoV-2 NSP4 T492I mutation promotes double-membrane vesicle formation to facilitate transmission. *Virol. Sin.* **40**, 225–235 (2025).

121. Chen, C. *et al.* Overview of antiviral drug candidates targeting coronaviral 3C-like main proteases. *FEBS J.* **288**, 5089–5121 (2021).

122. Cottam, E. M. *et al.* Coronavirus nsp6 proteins generate autophagosomes from the endoplasmic reticulum via an omegasome intermediate. *Autophagy* **7**, 1335–1347 (2011).

123. Nishitsuji, H., Iwahori, S., Ohmori, M., Shimotohno, K. & Murata, T. Ubiquitination of SARS-CoV-2 NSP6 and ORF7a Facilitates NF-κB Activation. *mBio* **13**, e00971-22 (2022).

124. Singh, D. *et al.* Redefining NSP12 activity in SARS-CoV-2 and its regulation by NSP8 and NSP7. *Mol. Ther. Nucleic Acids* **36**, 102452 (2025).

125. Biswal, M. *et al.* Two conserved oligomer interfaces of NSP7 and NSP8 underpin the dynamic assembly of SARS-CoV-2 RdRP. *Nucleic Acids Res.* **49**, 5956–5966 (2021).

126. Zhang, X. *et al.* SARS-CoV-2 Nsp8 suppresses MDA5 antiviral immune responses by impairing TRIM4-mediated K63-linked polyubiquitination. *PLOS Pathog.* **19**, e1011792 (2023).

127. Deng, J. *et al.* SARS-CoV-2 NSP8 suppresses type I and III IFN responses by modulating the RIG-I/MDA5, TRIF, and STING signaling pathways. *J. Med. Virol.* **95**, e28680 (2023).

128. Lundrigan, E., Toudic, C., Pennock, E. & Pezacki, J. P. SARS-CoV-2 Protein Nsp9 Is Involved in Viral Evasion through Interactions with Innate Immune Pathways. *ACS Omega* **9**, 26428–26438 (2024).

129. Gorkhali, R. *et al.* Structure and Function of Major SARS-CoV-2 and SARS-CoV Proteins. *Bioinforma. Biol. Insights* **15**, 11779322211025876 (2021).

130. Bhardwaj, T. *et al.* Amyloidogenic proteins in the SARS-CoV and SARS-CoV-2 proteomes. *Nat. Commun.* **14**, 945 (2023).

131. Gadhave, K. *et al.* Conformational dynamics of 13 amino acids long NSP11 of SARS-CoV-2 under membrane mimetics and different solvent conditions. *Microb. Pathog.* **158**, 105041 (2021).

132. Eastman, R. T. *et al.* Remdesivir: A Review of Its Discovery and Development Leading to Emergency Use Authorization for Treatment of COVID-19. *ACS Cent. Sci.* **6**, 672–683 (2020).

133. Robson, F. *et al.* Coronavirus RNA Proofreading: Molecular Basis and Therapeutic Targeting. *Mol. Cell* **79**, 710–727 (2020).

134. Kim, Y. *et al.* Tipiracil binds to uridine site and inhibits Nsp15 endoribonuclease NendoU from SARS-CoV-2. *Commun. Biol.* **4**, 193 (2021).

135. Misra, A. *et al.* Structural insights into the assembly and regulation of 2′-O RNA methylation by SARS-CoV-2 nsp16/nsp10. *Structure* **33**, 1027-1039.e4 (2025).

136. Han, L. *et al.* SARS-CoV-2 ORF10 antagonizes STING-dependent interferon activation and autophagy. *J. Med. Virol.* **94**, 5174–5188 (2022).

137. Li, X. *et al.* SARS-CoV-2 ORF10 suppresses the antiviral innate immune response by degrading MAVS through mitophagy. *Cell. Mol. Immunol.* **19**, 67–78 (2022).

138. Rashid, F., Dzakah, E. E., Wang, H. & Tang, S. The ORF8 protein of SARS-CoV-2 induced endoplasmic reticulum stress and mediated immune evasion by antagonizing production of interferon beta. *Virus Res.* **296**, 198350 (2021).

139. Zhang, Y. *et al.* The SARS-CoV-2 protein ORF3a inhibits fusion of autophagosomes with lysosomes. *Cell Discov.* **7**, 31 (2021).

140. Hou, P. *et al.* The ORF7a protein of SARS-CoV-2 initiates autophagy and limits autophagosome-lysosome fusion via degradation of SNAP29 to promote virus replication. *Autophagy* **19**, 551–569 (2023).

141. Walia, K. *et al.* SARS-CoV-2 virulence factor ORF3a blocks lysosome function by modulating TBC1D5-dependent Rab7 GTPase cycle. *Nat. Commun.* **15**, 2053 (2024).

142. Michelucci, A. *et al.* SARS-CoV-2 ORF3a accessory protein is a water-permeable channel that induces lysosome swelling. *Commun. Biol.* **8**, 170 (2025).

143. Kern, D. M. *et al.* Cryo-EM structure of SARS-CoV-2 ORF3a in lipid nanodiscs. *Nat. Struct. Mol. Biol.* **28**, 573–582 (2021).

144. Miller, A. N. *et al.* The SARS-CoV-2 accessory protein Orf3a is not an ion channel, but does interact with trafficking proteins. *eLife* **12**, e84477 (2023).

145. Cao, Z. *et al.* Ubiquitination of SARS-CoV-2 ORF7a promotes antagonism of interferon response. *Cell. Mol. Immunol.* **18**, 746–748 (2021).

146. Mari, M. *et al.* An Atg9-containing compartment that functions in the early steps of autophagosome biogenesis. *J. Cell Biol.* **190**, 1005–1022 (2010).

147. Mattera, R., Park, S. Y., De Pace, R., Guardia, C. M. & Bonifacino, J. S. AP-4 mediates export of ATG9A from the *trans* -Golgi network to promote autophagosome formation. *Proc. Natl. Acad. Sci.* **114**, (2017).

148. Sawa-Makarska, J. *et al.* Reconstitution of autophagosome nucleation defines Atg9 vesicles as seeds for membrane formation. *Science* **369**, eaaz7714 (2020).

149. Mizushima, N. The ATG conjugation systems in autophagy. *Curr. Opin. Cell Biol.* **63**, 1–10 (2020).

150. Melia, T. J., Lystad, A. H. & Simonsen, A. Autophagosome biogenesis: From membrane growth to closure. *J. Cell Biol.* **219**, e202002085 (2020).

151. Nähse, V., Stenmark, H. & Schink, K. O. Omegasomes control formation, expansion, and closure of autophagosomes. *BioEssays* **46**, 2400038 (2024).

152. Axe, E. L. *et al.* Autophagosome formation from membrane compartments enriched in phosphatidylinositol 3-phosphate and dynamically connected to the endoplasmic reticulum. *J. Cell Biol.* **182**, 685–701 (2008).

153. Polson, H. E. J. *et al.* Mammalian Atg18 (WIPI2) localizes to omegasome-anchored phagophores and positively regulates LC3 lipidation. *Autophagy* **6**, 506–522 (2010).

154. Lazarou, M. *et al.* The ubiquitin kinase PINK1 recruits autophagy receptors to induce mitophagy. *Nature* **524**, 309–314 (2015).

155. Nähse, V. *et al.* ATPase activity of DFCP1 controls selective autophagy. *Nat. Commun.* **14**, 4051 (2023).

156. Kumar, S. *et al.* Phosphorylation of Syntaxin 17 by TBK1 Controls Autophagy Initiation. *Dev. Cell* **49**, 130-144.e6 (2019).

157. Maeda, S., Otomo, C. & Otomo, T. The autophagic membrane tether ATG2A transfers lipids between membranes. *eLife* **8**, e45777 (2019).

158. Osawa, T. *et al.* Atg2 mediates direct lipid transfer between membranes for autophagosome formation. *Nat. Struct. Mol. Biol.* **26**, 281–288 (2019).

159. Matoba, K. *et al.* Atg9 is a lipid scramblase that mediates autophagosomal membrane expansion. *Nat. Struct. Mol. Biol.* **27**, 1185–1193 (2020).

160. Maeda, S. *et al.* Structure, lipid scrambling activity and role in autophagosome formation of ATG9A. *Nat. Struct. Mol. Biol.* **27**, 1194–1201 (2020).

161. Wang, Y. *et al.* Structural basis for lipid transfer by the ATG2A–ATG9A complex. *Nat. Struct. Mol. Biol.* **32**, 35–47 (2025).

162. Moretti, F. *et al.* TMEM 41B is a novel regulator of autophagy and lipid mobilization. *EMBO Rep.* **19**, e45889 (2018).

163. Li, Y. E. *et al.* TMEM41B and VMP1 are scramblases and regulate the distribution of cholesterol and phosphatidylserine. *J. Cell Biol.* **220**, e202103105 (2021).

164. Gómez-Sánchez, R. *et al.* Atg9 establishes Atg2-dependent contact sites between the endoplasmic reticulum and phagophores. *J. Cell Biol.* **217**, 2743–2763 (2018).

165. Kotani, T., Kirisako, H., Koizumi, M., Ohsumi, Y. & Nakatogawa, H. The Atg2-Atg18 complex tethers pre-autophagosomal membranes to the endoplasmic reticulum for autophagosome formation. *Proc. Natl. Acad. Sci.* **115**, 10363–10368 (2018).

166. Valverde, D. P. *et al.* ATG2 transports lipids to promote autophagosome biogenesis. *J. Cell Biol.* **218**, 1787–1798 (2019).

167. Vargas Duarte, P. & Reggiori, F. The Organization and Function of the Phagophore-ER Membrane Contact Sites. *Contact* **6**, 25152564231183898 (2023).

168. Proikas-Cezanne, T., Takacs, Z., Dönnes, P. & Kohlbacher, O. WIPI proteins: essential PtdIns3 *P* effectors at the nascent autophagosome. *J. Cell Sci.* jcs.146258 (2015) doi:10.1242/jcs.146258.

169. Mailler, E. *et al.* The autophagy protein ATG9A enables lipid mobilization from lipid droplets. *Nat. Commun.* **12**, 6750 (2021).

170. Shpilka, T. *et al.* Lipid droplets and their component triglycerides and steryl esters regulate autophagosome biogenesis. *EMBO J.* **34**, 2117–2131 (2015).

171. Andrejeva, G. *et al. De novo* phosphatidylcholine synthesis is required for autophagosome membrane formation and maintenance during autophagy. *Autophagy* **16**, 1044–1060 (2020).

172. Morita, K. *et al.* Genome-wide CRISPR screen identifies *TMEM41B* as a gene required for autophagosome formation. *J. Cell Biol.* **217**, 3817–3828 (2018).

173. Shoemaker, C. J. *et al.* CRISPR screening using an expanded toolkit of autophagy reporters identifies TMEM41B as a novel autophagy factor. *PLOS Biol.* **17**, e2007044 (2019).

174. Carlsson, S. R. & Simonsen, A. Membrane dynamics in autophagosome biogenesis. *J. Cell Sci.* jcs.141036 (2015) doi:10.1242/jcs.141036.

175. Agudo-Canalejo, J. & Knorr, R. L. Formation of Autophagosomes Coincides with Relaxation of Membrane Curvature. in *Autophagy* (eds Ktistakis, N. & Florey, O.) vol. 1880 173–188 (Springer New York, New York, NY, 2019).

176. Lystad, A. H. *et al.* Distinct functions of ATG16L1 isoforms in membrane binding and LC3B lipidation in autophagy-related processes. *Nat. Cell Biol.* **21**, 372–383 (2019).

177. Ichimura, Y. *et al.* A ubiquitin-like system mediates protein lipidation. *Nature* **408**, 488–492 (2000).

178. Zheng, Y. *et al.* A switch element in the autophagy E2 Atg3 mediates allosteric regulation across the lipidation cascade. *Nat. Commun.* **10**, 3600 (2019).

179. Schaaf, M. B. E., Keulers, T. G., Vooijs, M. A. & Rouschop, K. M. A. LC3/GABARAP family proteins: autophagy-(un)related functions. *FASEB J.* **30**, 3961–3978 (2016).

180. Weidberg, H. *et al.* LC3 and GATE-16 N Termini Mediate Membrane Fusion Processes Required for Autophagosome Biogenesis. *Dev. Cell* **20**, 444–454 (2011).

181. Johansen, T. & Lamark, T. Selective Autophagy: ATG8 Family Proteins, LIR Motifs and Cargo Receptors. *J. Mol. Biol.* **432**, 80–103 (2020).

182. He, H. *et al.* Post-translational Modifications of Three Members of the Human MAP1LC3 Family and Detection of a Novel Type of Modification for MAP1LC3B. *J. Biol. Chem.* **278**, 29278–29287 (2003).

183. Coelho, P. P. *et al.* Endosomal LC3C-pathway selectively targets plasma membrane cargo for autophagic degradation. *Nat. Commun.* **13**, 3812 (2022).

184. Huang, T. *et al.* MST4 Phosphorylation of ATG4B Regulates Autophagic Activity, Tumorigenicity, and Radioresistance in Glioblastoma. *Cancer Cell* **32**, 840-855.e8 (2017).

185. Kuang, E. *et al.* Regulation of ATG4B Stability by RNF5 Limits Basal Levels of Autophagy and Influences Susceptibility to Bacterial Infection. *PLoS Genet.* **8**, e1003007 (2012).

186. Jo, Y. K. *et al.* O-GlcNAcylation of ATG4B positively regulates autophagy by increasing its hydroxylase activity. *Oncotarget* **7**, 57186–57196 (2016).

187. Li, Y. *et al.* Autophagy impairment mediated by S-nitrosation of ATG4B leads to neurotoxicity in response to hyperglycemia. *Autophagy* **13**, 1145–1160 (2017).

188. Pérez-Pérez, M. E., Zaffagnini, M., Marchand, C. H., Crespo, J. L. & Lemaire, S. D. The yeast autophagy protease Atg4 is regulated by thioredoxin. *Autophagy* **10**, 1953–1964 (2014).

189. Scherz-Shouval, R. *et al.* Reactive oxygen species are essential for autophagy and specifically regulate the activity of Atg4. *EMBO J.* **26**, 1749–1760 (2007).

190. Herhaus, L. *et al.* TBK1-mediated phosphorylation of LC3C and GABARAP-L2 controls autophagosome shedding by ATG4 protease. *EMBO Rep.* **21**, e48317 (2020).

191. Engedal, N. & Seglen, P. O. Autophagy of cytoplasmic bulk cargo does not require LC3. *Autophagy* **12**, 439–441 (2016).

192. Tsuboyama, K. *et al.* The ATG conjugation systems are important for degradation of the inner autophagosomal membrane. *Science* **354**, 1036–1041 (2016).

193. Nguyen, T. N. *et al.* Atg8 family LC3/GABARAP proteins are crucial for autophagosome–lysosome fusion but not autophagosome formation during PINK1/Parkin mitophagy and starvation. *J. Cell Biol.* **215**, 857–874 (2016).

194. Weidberg, H. *et al.* LC3 and GATE-16/GABARAP subfamilies are both essential yet act differently in autophagosome biogenesis. *EMBO J.* **29**, 1792–1802 (2010).

195. Nakatogawa, H., Ishii, J., Asai, E. & Ohsumi, Y. Atg4 recycles inappropriately lipidated Atg8 to promote autophagosome biogenesis. *Autophagy* **8**, 177–186 (2012).

196. Nguyen, T. N., Padman, B. S. & Lazarou, M. ATG4s: above and beyond the Atg8-family protein lipidation system. *Autophagy* **17**, 2648–2650 (2021).

197. Nguyen, T. N. *et al.* ATG4 family proteins drive phagophore growth independently of the LC3/GABARAP lipidation system. *Mol. Cell* **81**, 2013-2030.e9 (2021).

198. Kauffman, K. J. *et al.* Delipidation of mammalian Atg8-family proteins by each of the four ATG4 proteases. *Autophagy* 1–19 (2018) doi:10.1080/15548627.2018.1437341.

199. Li, M. *et al.* Kinetics Comparisons of Mammalian Atg4 Homologues Indicate Selective Preferences toward Diverse Atg8 Substrates. *J. Biol. Chem.* **286**, 7327–7338 (2011).

200. Tamargo-Gómez, I. *et al.* ATG4D is the main ATG8 delipidating enzyme in mammalian cells and protects against cerebellar neurodegeneration. *Cell Death Differ.* **28**, 2651–2672 (2021).

201. Tamargo-Gómez, I. *et al.* Analysis of ATG4C function *in vivo*. *Autophagy* **19**, 2912–2933 (2023).

202. Norman, J. M., Cohen, G. M. & Bampton, E. T. W. The in vitro cleavage of the hAtg proteins by cell death proteases. *Autophagy* **6**, 1042–1056 (2010).

203. Betin, V. M. S. & Lane, J. D. Caspase cleavage of Atg4D stimulates GABARAP-L1 processing and triggers mitochondrial targeting and apoptosis. *J. Cell Sci.* **122**, 2554–2566 (2009).

204. Betin, V. M. S. & Lane, J. D. Atg4D at the interface between autophagy and apoptosis. *Autophagy* **5**, 1057–1059 (2009).

205. Agrotis, A., Pengo, N., Burden, J. J. & Ketteler, R. Redundancy of human ATG4 protease isoforms in autophagy and LC3/GABARAP processing revealed in cells. *Autophagy* **15**, 976–997 (2019).

206. Morimoto, M. *et al.* Bi-allelic ATG4D variants are associated with a neurodevelopmental disorder characterized by speech and motor impairment. *Npj Genomic Med.* **8**, 4 (2023).

207. Durgan, J. *et al.* Non-canonical autophagy drives alternative ATG8 conjugation to phosphatidylserine. *Mol. Cell* **81**, 2031-2040.e8 (2021).

208. Betin, V. M. S., MacVicar, T. D. B., Parsons, S. F., Anstee, D. J. & Lane, J. D. A cryptic mitochondrial targeting motif in Atg4D links caspase cleavage with mitochondrial import and oxidative stress. *Autophagy* **8**, 664–676 (2012).

209. McMann, E. & Gorski, S. M. Last but not least: emerging roles of the autophagy-related protein ATG4D. *Autophagy* **20**, 1916–1927 (2024).

210. Knorr, R. L., Lipowsky, R. & Dimova, R. Autophagosome closure requires membrane scission. *Autophagy* **11**, 2134–2137 (2015).

211. Takahashi, Y. *et al.* An autophagy assay reveals the ESCRT-III component CHMP2A as a regulator of phagophore closure. *Nat. Commun.* **9**, 2855 (2018).

212. Takahashi, Y. *et al.* VPS37A directs ESCRT recruitment for phagophore closure. *J. Cell Biol.* **218**, 3336–3354 (2019).

213. Zhou, F. *et al.* Rab5-dependent autophagosome closure by ESCRT. *J. Cell Biol.* **218**, 1908–1927 (2019).

214. Zhen, Y. *et al.* ESCRT-mediated phagophore sealing during mitophagy. *Autophagy* **16**, 826–841 (2020).

215. Vergne, I. & Deretic, V. The role of PI3P phosphatases in the regulation of autophagy. *FEBS Lett.* **584**, 1313–1318 (2010).

216. Lőrincz, P. & Juhász, G. Autophagosome-Lysosome Fusion. *J. Mol. Biol.* **432**, 2462–2482 (2020).

217. Kemball, C. C. *et al.* Coxsackievirus Infection Induces Autophagy-Like Vesicles and Megaphagosomes in Pancreatic Acinar Cells *In Vivo*. *J. Virol.* **84**, 12110–12124 (2010).

218. Choi, Y., Bowman, J. W. & Jung, J. U. Autophagy during viral infection — a double-edged sword. *Nat. Rev. Microbiol.* **16**, 341–354 (2018).

219. Jassey, A. & Jackson, W. T. Viruses and autophagy: bend, but don't break. *Nat. Rev. Microbiol.* **22**, 309–321 (2024).

220. Zhou, X. *et al.* Quantitative Proteomic Analysis of Porcine Intestinal Epithelial Cells Infected with Porcine Deltacoronavirus Using iTRAQ-Coupled LC-MS/MS. *J. Proteome Res.* **19**, 4470–4485 (2020).

221. Reggiori, F. *et al.* Coronaviruses Hijack the LC3-I-Positive EDEMosomes, ER-Derived Vesicles Exporting Short-Lived ERAD Regulators, for Replication. *Cell Host Microbe* **7**, 500–508 (2010).

222. Zou, D. *et al.* Porcine epidemic diarrhea virus ORF3 protein causes endoplasmic reticulum stress to facilitate autophagy. *Vet. Microbiol.* **235**, 209–219 (2019).

223. Lin, H. *et al.* Nonstructural protein 6 of porcine epidemic diarrhea virus induces autophagy to promote viral replication via the PI3K/Akt/mTOR axis. *Vet. Microbiol.* **244**, 108684 (2020).

224. Tabata, K. *et al.* Convergent use of phosphatidic acid for hepatitis C virus and SARS-CoV-2 replication organelle formation. *Nat. Commun.* **12**, 7276 (2021).

225. Hui, X. *et al.* SARS-CoV-2 promote autophagy to suppress type I interferon response. *Signal Transduct. Target. Ther.* **6**, 180 (2021).

226. Li, F. *et al.* SARS-CoV-2 spike promotes inflammation and apoptosis through autophagy by ROS-suppressed PI3K/AKT/mTOR signaling. *Biochim. Biophys. Acta BBA - Mol. Basis Dis.* **1867**, 166260 (2021).

227. Gassen, N. C. *et al.* SARS-CoV-2-mediated dysregulation of metabolism and autophagy uncovers host-targeting antivirals. *Nat. Commun.* **12**, 3818 (2021).

228. Su, W., Yu, X. & Zhou, C. SARS-CoV-2 ORF3a Induces Incomplete Autophagy via the Unfolded Protein Response. *Viruses* **13**, 2467 (2021).

229. Koči, J., Novotová, M., Sláviková, M., Klempa, B. & Zahradník, I. SARS-CoV-2 Exploits Non-Canonical Autophagic Processes to Replicate, Mature, and Egress the Infected Vero E6 Cells. *Pathogens* **11**, 1535 (2022).

230. Sui, C. *et al.* SARS-CoV-2 NSP13 Inhibits Type I IFN Production by Degradation of TBK1 via p62-Dependent Selective Autophagy. *J. Immunol.* **208**, 753–761 (2022).

231. Barbati, C. *et al.* Autophagy Hijacking in PBMC From COVID-19 Patients Results in Lymphopenia. *Front. Immunol.* **13**, 903498 (2022).

232. Sanjana, N. E., Shalem, O. & Zhang, F. Improved vectors and genome-wide libraries for CRISPR screening. *Nat. Methods* **11**, 783–784 (2014).

233. Pahmeier, F. *et al.* Identification of host dependency factors involved in SARS-CoV-2 replication organelle formation through proteomics and ultrastructural analysis. *J. Virol.* **97**, e00878-23 (2023).

234. Ishibashi, K. *et al.* Atg16L2, a novel isoform of mammalian Atg16L that is not essential for canonical autophagy despite forming an Atg12–5-16L2 complex. *Autophagy* **7**, 1500–1513 (2011).

235. Tamura, N., Oku, M. & Sakai, Y. Atg8 regulates vacuolar membrane dynamics in a lipidation-independent manner in *Pichia pastoris*. *J. Cell Sci.* **123**, 4107–4116 (2010).

236. Maeda, Y., Oku, M. & Sakai, Y. Autophagy-independent function of Atg8 in lipid droplet dynamics in yeast. *J. Biochem. (Tokyo)* mvw078 (2016) doi:10.1093/jb/mvw078.

237. Goyal, U. & Blackstone, C. Untangling the web: Mechanisms underlying ER network formation. *Biochim. Biophys. Acta BBA - Mol. Cell Res.* **1833**, 2492–2498 (2013).

238. Park, S. H. & Blackstone, C. Further assembly required: construction and dynamics of the endoplasmic reticulum network. *EMBO Rep.* **11**, 515–521 (2010).

239. Voeltz, G. K., Prinz, W. A., Shibata, Y., Rist, J. M. & Rapoport, T. A. A Class of Membrane Proteins Shaping the Tubular Endoplasmic Reticulum. *Cell* **124**, 573–586 (2006).

240. Rismanchi, N., Soderblom, C., Stadler, J., Zhu, P.-P. & Blackstone, C. Atlastin GTPases are required for Golgi apparatus and ER morphogenesis. *Hum. Mol. Genet.* **17**, 1591–1604 (2008).

241. Hu, J. *et al.* A Class of Dynamin-like GTPases Involved in the Generation of the Tubular ER Network. *Cell* **138**, 549–561 (2009).

242. Orso, G. *et al.* Homotypic fusion of ER membranes requires the dynamin-like GTPase Atlastin. *Nature* **460**, 978–983 (2009).

243. Wang, S., Tukachinsky, H., Romano, F. B. & Rapoport, T. A. Cooperation of the ER-shaping proteins atlastin, lunapark, and reticulons to generate a tubular membrane network. *eLife* **5**, e18605 (2016).

244. Zhao, Y., Zhang, T., Huo, H., Ye, Y. & Liu, Y. Lunapark Is a Component of a Ubiquitin Ligase Complex Localized to the Endoplasmic Reticulum Three-way Junctions. *J. Biol. Chem.* **291**, 18252–18262 (2016).

245. Anggrandariyanny, P. C., Kajiho, H., Yamamoto, Y. & Sakisaka, T. Lunapark ubiquitinates atlastin-2 for the tubular network formation of the endoplasmic reticulum. *J. Biochem. (Tokyo)* **172**, 245–257 (2022).

246. Klemm, R. W. *et al.* A Conserved Role for Atlastin GTPases in Regulating Lipid Droplet Size. *Cell Rep.* **3**, 1465–1475 (2013).

247. Bian, X. *et al.* Structures of the atlastin GTPase provide insight into homotypic fusion of endoplasmic reticulum membranes. *Proc. Natl. Acad. Sci.* **108**, 3976–3981 (2011).

248. Byrnes, L. J. *et al.* Structural basis for conformational switching and GTP loading of the large G protein atlastin. *EMBO J.* **32**, 369–384 (2013).

249. Byrnes, L. J. & Sondermann, H. Structural basis for the nucleotide-dependent dimerization of the large G protein atlastin-1/SPG3A. *Proc. Natl. Acad. Sci.* **108**, 2216–2221 (2011).

250. Jang, E. *et al.* Human atlastins are sufficient to drive the fusion of liposomes with a physiological lipid composition. *J. Cell Biol.* **222**, e202109090 (2023).

251. Hu, X., Wu, F., Sun, S., Yu, W. & Hu, J. Human atlastin GTPases mediate differentiated fusion of endoplasmic reticulum membranes. *Protein Cell* **6**, 307–311 (2015).

252. Liang, J. R., Lingeman, E., Ahmed, S. & Corn, J. E. Atlastins remodel the endoplasmic reticulum for selective autophagy. *J. Cell Biol.* **217**, 3354–3367 (2018).

253. Neufeldt, C. J. *et al.* ER-shaping atlastin proteins act as central hubs to promote flavivirus replication and virion assembly. *Nat. Microbiol.* **4**, 2416–2429 (2019).

254. Chen, Q. *et al.* ATL3 Is a Tubular ER-Phagy Receptor for GABARAP-Mediated Selective Autophagy. *Curr. Biol.* **29**, 846-855.e6 (2019).

255. Liu, N., Zhao, H., Zhao, Y. G., Hu, J. & Zhang, H. Atlastin 2/3 regulate ER targeting of the ULK1 complex to initiate autophagy. *J. Cell Biol.* **220**, e202012091 (2021).

256. Crosby, D. *et al.* Reconstitution of human atlastin fusion activity reveals autoinhibition by the C terminus. *J. Cell Biol.* **221**, e202107070 (2022).

257. Bryce, S. *et al.* Human atlastin-3 is a constitutive ER membrane fusion catalyst. *J. Cell Biol.* **222**, e202211021 (2023).